IMMUNODEFICIENCY

The cytoskeletal regulator HEM1 governs B cell development and prevents autoimmunity

Elisabeth Salzer[1,2,3,4]*, Samaneh Zoghi[1,2,3,5,6]*, Máté G. Kiss[3,7†], Frieda Kage[8,9†], Christina Rashkova[1,3,10†], Stephanie Stahnke[9†], Matthias Haimel[1,2,3†], René Platzer[11], Michael Caldera[3], Rico Chandra Ardy[1,2,3], Birgit Hoeger[1,2,3], Jana Block[1,2,3], David Medgyesi[1], Celine Sin[3], Sepideh Shahkarami[5,12,13], Renate Kain[14], Vahid Ziaee[15,16], Peter Hammerl[17‡], Christoph Bock[1,3], Jörg Menche[3], Loïc Dupré[1,18], Johannes B. Huppa[11], Michael Sixt[19], Alexis Lomakin[1,2,3], Klemens Rottner[8,9], Christoph J. Binder[3,7], Theresia E. B. Stradal[9], Nima Rezaei[5,6,20], Kaan Boztug[2,1,3,4,10§]

The WAVE regulatory complex (WRC) is crucial for assembly of the peripheral branched actin network constituting one of the main drivers of eukaryotic cell migration. Here, we uncover an essential role of the hematopoietic-specific WRC component HEM1 for immune cell development. Germline-encoded HEM1 deficiency underlies an inborn error of immunity with systemic autoimmunity, at cellular level marked by WRC destabilization, reduced filamentous actin, and failure to assemble lamellipodia. Hem1$^{-/-}$ mice display systemic autoimmunity, phenocopying the human disease. In the absence of Hem1, B cells become deprived of extracellular stimuli necessary to maintain the strength of B cell receptor signaling at a level permissive for survival of non-autoreactive B cells. This shifts the balance of B cell fate choices toward autoreactive B cells and thus autoimmunity.

INTRODUCTION

The actin cytoskeleton is fundamental to mount successful immune responses, as evident from the wide range of defects that occur in actin-related inborn errors of immunity (*1*–*4*). Studies of these conditions have revealed a pivotal role for the actin cytoskeleton and actin-binding proteins in immune system function: from hematopoiesis and immune cell development to immune cell migration to intercellular and intracellular signaling including immune cell activation (*1*).

The actin cytoskeleton is composed of networks and bundles of actin filaments (F-actin) that are polymerized from actin monomers, e.g., underneath the plasma membrane. The polymerization is initiated by the three classes of actin nucleators, the Arp2/3 complex, the formin family, and the more recently identified Spire, cordon-bleu, and leiomodin family proteins (*5*). Formins nucleate and elongate linear actin filaments, whereas the Arp2/3 complex drives filament branch formation on preexisting filaments (*6*). The Wiskott-Aldrich syndrome protein (WASP) and WASP family verprolin-homologous (WAVE) family proteins promote F-actin branching through the Arp2/3 complex. WAVE proteins form a 400-kDa heteropentameric (*7*–*9*) assembly called the WAVE regulatory complex (WRC). WRC-deficient cells are unable to generate lamellipodia or membrane ruffles, and Wave2 knockout (KO) mice are embryonic lethal because of impaired endothelial cell migration (*10*). Most studies of actin-related immunodeficiencies typically attribute abnormalities in the locomotory cell apparatus per se to the key pathogenic mechanism (*1*–*3*, *11*). At the same time, recent data from nonimmune cell types strongly suggest that cell-scale actin cytoskeleton morphodynamics control the spatiotemporal output and the intensity of signaling events at the molecular level (*12*, *13*). However, the scale-bridging mechanisms linking signaling events and actin cytoskeleton–mediated cell morphogenetic behaviors remain largely unexplored in the context of immune cell physiology and pathobiology.

Here, we find that WRC deficiency caused by the absence of the WRC hematopoietic cell–specific subunit HEM1 results in a previously unknown human disorder with severe immune dysregulation and recurrent infections. By studying the molecular and cellular mechanisms behind this inborn error of immunity, we uncover HEM1 as a key regulator of B cell receptor (BCR) signaling strength that is crucial for B cell development and homeostasis.

RESULTS

Identification of human HEM1 deficiency

We studied two patients with recurrent fever with and without signs of infection from the age of 4 months (Fig. 1A). Patient 1 (P1)

[1]Ludwig Boltzmann Institute for Rare and Undiagnosed Diseases, Vienna, Austria. [2]St. Anna Children's Cancer Research Institute (CCRI), Vienna, Austria. [3]CeMM Research Center for Molecular Medicine of the Austrian Academy of Sciences, Vienna, Austria. [4]St. Anna Children's Hospital, Department of Pediatrics and Adolescent Medicine, Medical University of Vienna, Vienna, Austria. [5]Research Center for Immunodeficiencies, Children's Medical Center, Tehran University of Medical Sciences, Tehran, Iran. [6]Department of Immunology, School of Medicine, Tehran University of Medical Sciences, Tehran, Iran. [7]Department of Laboratory Medicine, Medical University of Vienna, Vienna, Austria. [8]Division of Molecular Cell Biology, Zoological Institute, Technische Universität Braunschweig, Braunschweig, Germany. [9]Department of Cell Biology, Helmholtz Centre for Infection Research, Braunschweig, Germany. [10]Department of Pediatrics and Adolescent Medicine, Medical University of Vienna, Vienna, Austria. [11]Institute for Hygiene and Applied Immunology, Center for Pathophysiology, Infectiology and Immunology, Medical University of Vienna, Vienna, Austria. [12]Department of Medical Genetics, School of Medicine, Tehran University of Medical Sciences, Tehran, Iran. [13]Medical Genetics Network (MeGeNe), Universal Scientific Education and Research Network (USERN), Tehran, Iran. [14]Department of Pathology, Medical University of Vienna, Vienna, Austria. [15]Pediatric Rheumatology Research Group, Rheumatology Research Center, Tehran University of Medical Sciences, Tehran, Iran. [16]Department of Pediatrics, Tehran University of Medical Sciences, Tehran, Iran. [17]Department of Molecular Biology, University of Salzburg, Salzburg, Austria. [18]Center for Pathophysiology of Toulouse Purpan, INSERM UMR1043, CNRS UMR5282, Paul Sabatier University, Toulouse, France. [19]Institute of Science and Technology Austria, Klosterneuburg, Austria. [20]Network of Immunity in Infection, Malignancy and Autoimmunity (NIIMA), Universal Scientific Education and Research Network (USERN), Tehran, Iran.
*These authors contributed equally to this work.
†These authors contributed equally to this work.
‡Deceased.
§Corresponding author. Email: kaan.boztug@ccri.at

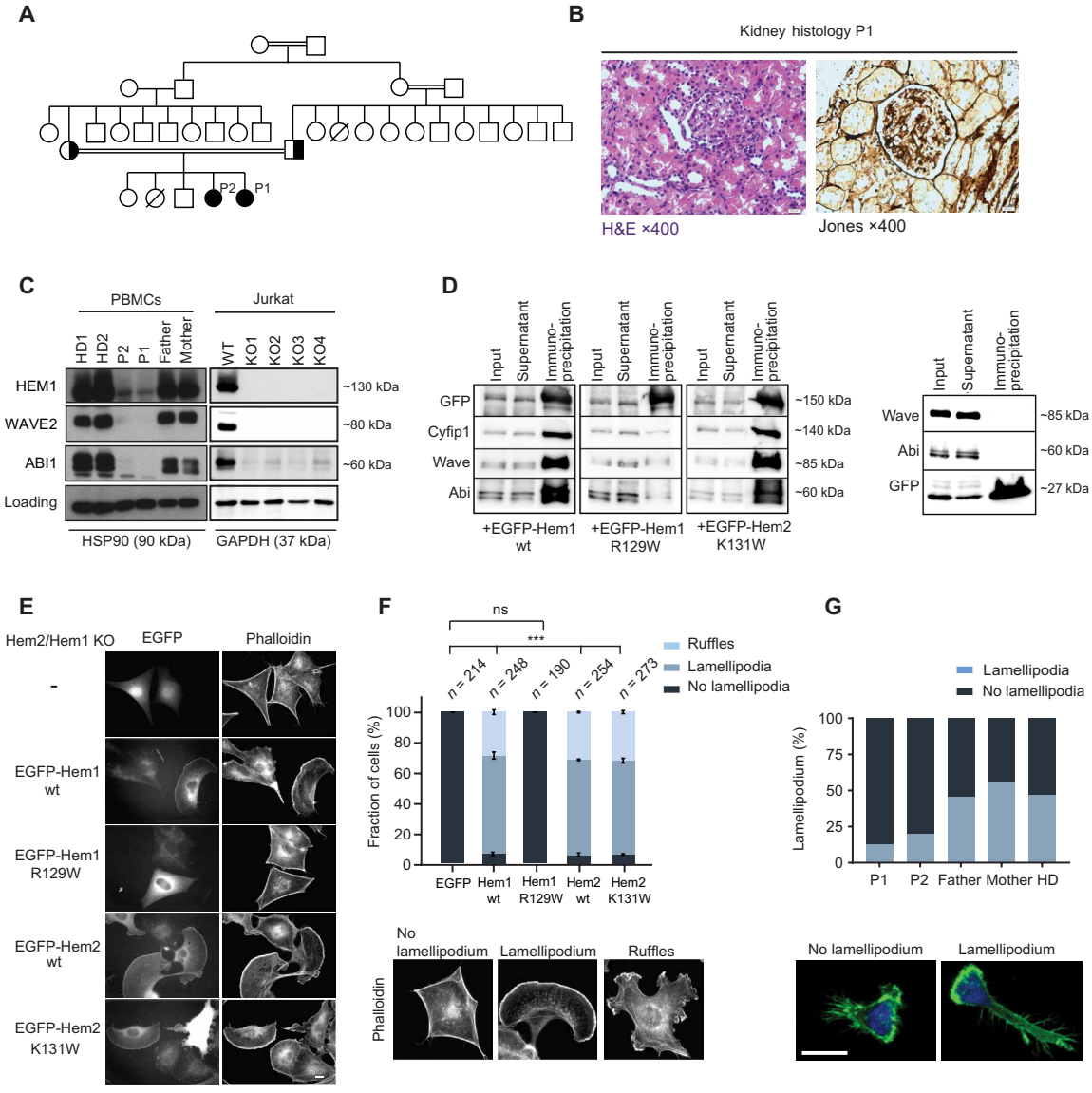

Fig. 1. HEM1 deficiency results in aberrant cell morphology and defective lamellipodia formation in HEM1-deficient patients. (**A**) Pedigree of the index family: Double lines, consanguinity; black filling, the index patients; diagonal lines, deceased siblings. (**B**) Image of hematoxylin and eosin (H&E) staining showing capillary proliferation and polymorphonuclear neutrophils in glomeruli (magnification, ×400) (left) and periodic acid–Schiff (PAS) staining showing mild mesangial expansion (magnification, ×400) (right), consistent with lupus nephritis, class III, active. (**C**) Cropped immunoblot analysis of HEM1, WAVE2, ABI1, GAPDH (glyceraldehyde phosphate dehydrogenase), or HSP90 (heat shock protein 90) in PBMCs of healthy donor (HD), patients (P1 and P2), and their parents (left) and in CRISPR-Cas9 *HEM1* KO Jurkat T cells (right). (**D**) Co-immunoprecipitation of endogenous WRC subunits with ectopically expressed EGFP-tagged proteins (indicated at the bottom) in wt B16-F1 cells. EGFP alone was used as control (right). (**E**) Hem2/Hem1 KO B16-F1 clone #8 was transfected with indicated EGFP-tagged constructs. The panels display respective phalloidin stainings. Scale bar, 10 μm. (**F**) Quantification of lamellipodia/ruffle formation as indicated by the color shading shows fraction of cells in percentage ± SEM from three independent experiments. *n* equals number of transfected cells analyzed. Bottom: Representative examples of cell morphologies used for cell categorization. (**G**) Representative images (bottom) and quantification (top) of expanded T cells spreading on fibronectin-coated surfaces stained with phalloidin and 4′,6-diamidino-2-phenylindole (DAPI) and imaged with a Zeiss LSM700 confocal microscope and a 63× oil immersion objective. Scale bar, 10 μm. ns, not significant.

experienced multiple upper respiratory tract infections and later developed skin rashes, oral ulcers, photosensitivity, joint pain, fatigue, and glomerulonephritis (Fig. 1B and fig. S1A). She was tested positive for anti–double-stranded DNA (dsDNA) antibodies and diagnosed with systemic lupus erythematosus (SLE) according to current American College of Rheumatology (ACR) criteria (*14*). The patient exhibited failure to thrive with both height and weight below the third percentile. She has stable disease with long-term immunosuppression including corticosteroids and azathioprin. P1's 8-year-old sister (P2) has experienced recurrent infections since the first year of life. Glucose-6-phosphate dehydrogenase (G6PD) deficiency (*15*) was diagnosed but did not result in severe hemolytic events. P2 had recurrent respiratory tract infections, repeated skin abscesses, and multiple ear infections resulting in tympanic membrane perforation and unilateral hearing loss. Recurrent lymphadenopathy and fever were evident independent of (overt) infections. Periodic fever syndromes were

considered, but no germline mutation in *MEFV* indicative of familial Mediterranean fever (*16*) was detected. P2 has remained negative for anti-dsDNA autoantibodies to date and does not take medications regularly, but was treated with antibiotics repeatedly for assumed or proven bacterial infections. An older sister of P1 and P2 had died 2 hours postpartum of unknown cause without tissue samples available for molecular investigation.

To figure out the molecular basis of this disease, we performed exome sequencing (ES) of P1 and identified a conserved, homozygous missense variant (c.C385T, p.R129W) in the gene *NCKAP1L* encoding HEM1. Genetic segregation analysis revealed perfect segregation under the assumption of autosomal recessive inheritance including homozygosity for the affected sibling P2 (Fig. 1A and fig. S1, B and C). *NCKAP1L* was the only gene with homozygous variants shared among the two affected siblings. The identified variant has not been reported in public databases including ExAC (*17*) or gnomAD (*18*) (accession date: 1 January 2020) and is predicted highly damaging using prediction tools including CADD (combined annotation dependent depletion) (https://cadd.gs.washington.edu; accession date: 1 January 2020). No rare homozygous premature nonsense or frameshift variants in *NCKAP1L* have been reported in gnomAD or other publicly available databases. The probability of cellular intolerance to a loss-of-function mutation (pLI) score of 0.85 for *NCKAP1L* suggests that this gene may be essential for human health. Collectively, these observations gave strong support for *HEM1* as a promising candidate gene for the syndrome investigated.

Defective WRC assembly and stability

To examine the effect of the identified gene variant on protein expression, we performed immunoblotting in the following patient-derived cells: peripheral blood mononuclear cells (PBMCs) (Fig. 1C), feeder-expanded T cells, and Epstein-Barr virus (EBV)–immortalized B cells (EBV-LCL) (fig. S1, D and E), and we consistently observed markedly reduced HEM1 protein expression. Furthermore, the expression of the catalytic component WAVE2 and other subunits of the WRC were severely reduced in patient cells, illustrating a detrimental effect of the loss of HEM1 expression on the WRC assembly and stability. CRISPR-Cas9–engineered HEM1-deficient Jurkat T cells recapitulated the expression patterns observed in patient cells (Fig. 1C; all Western blot raw data can be found at the end of the Supplementary Materials).

Nonhematopoietic cells express the homologous protein HEM2 instead of HEM1 (*19*). In contrast to previous observations (*20*), recent work has suggested that compensatory HEM1 expression can, in principle, substitute for HEM2 expression (*21*). HEM2 and HEM1 share about 60% sequence homology. However, the arginine residue at position 129 in HEM1 is not conserved in HEM2, because the respective amino acid in HEM2 is shifted by two residues due to an upstream insertion and constitutes a lysine (instead of arginine) at position 131. The respective murine sequences are highly conserved, including R129 in Hem1 (fig. S1C).

To dissect the functional consequences of the R129W mutation in Hem1 and potential effects of the corresponding mutation in Hem2, we used the murine B16-F1 melanoma cell line as an established model system for actin remodeling and lamellipodium protrusion (*22*, *23*). We first performed co-immunoprecipitation experiments with enhanced green fluorescent protein (EGFP)–tagged, murine wild-type (wt) Hem1, Hem1-R129W, and the analogous mutation in Hem2, Hem2-K131W, using B16-F1 wt cells. Hem1-R129W showed strongly reduced coprecipitation of its interactors Cyfip1, Abi, and WAVE as compared with Hem1-wt or Hem2-K131W (Fig. 1D), already suggesting compromised interaction of Hem1-R129W with endogenous WRC subunits. However, degradation of mutant protein was not obvious under these conditions, likely because of excess production of transient, ectopic protein, as opposed to steady-state expression of the endogenous mutant variant in mouse or human patient tissue. Lamellipodia formation relies on a functional WRC (*24*, *25*). We thus hypothesized that the reduction of HEM1 and WAVE2 expression abrogates lamellipodia formation in Hem1-R129W–expressing patient cells. To test this, we engineered CRISPR-Cas9–edited Hem1/Hem2-deficient B16-F1 clones, which are completely devoid of lamellipodia (Fig. 1E, top panel). As opposed to EGFP expression alone, reexpression of EGFP-tagged Hem1-wt or Hem2-wt rescued lamellipodia (Fig. 1, E and F). Hem1-R129W expression failed to restore these structures, whereas the Hem2-K131W expression phenotype was virtually identical to that of Hem1-wt or Hem2-wt (Fig. 1, E and F). In contrast to Hem2-K131W, the Hem1-R129W protein was also unable to localize at subcellular sites normally occupied by Hem1-wt in B16-F1 wt cells, suggesting that the mutant Hem1 fails entirely to incorporate into functional WRCs (fig. S1F). Moreover, Hem1-R129W did not rescue lamellipodia formation in a second, independently generated Hem1/2 double-KO B16-F1 clone (fig. S1G). Consistently, cellular morphology in patient lymphocytes was aberrant, because they were unable to form stable lamellipodia and displayed reduced F-actin upon fibronectin stimulation (Fig. 1G and fig. S1, H to J). Instead, the cells showed signs of formin- and/or WASP-mediated F-actin structures with aberrant membrane spikes. Quantification of cell shape descriptors and subsequent principal components analysis (PCA) of the data showed a significant difference between patient and healthy donor T cells, with reduced cell spreading area being the most discriminative feature (fig. S1J; list of distinguishing features, table S2).

Impaired T cell function in HEM1 deficiency

Because HEM1 deficiency resulted in loss of lamellipodia and decreased cell spreading on the extracellular matrix (ECM), we investigated the physiological consequences of these abnormalities in the context of immune cell behavior. Hem1/2 and other subunits of the WRC are classically implicated in cell migration (*26*, *27*). However, when we examined immune cell migration efficiency using standard chemotaxis assays, we did not observe any remarkable differences between normal donor– and patient-derived cells (fig. S2A).

F-actin–mediated cell morphodynamics are also known to be crucially important for the effector/target cell conjugation and killing activity of cytolytic T cells (*28*). Nevertheless, our experiments showed that patient CD8 cells undergo normal activation (as mirrored by up-regulation of LFA-1 in both patient and CRISPR-Cas9–engineered HEM1-deficient Jurkat T cells) as well as intact conjugate formation toward OKT3-coated P815 cells (Fig. 2A and fig. S2B).

We nonetheless hypothesized that the cytoskeletal abnormalities observed in HEM1-deficient cells may perturb immune cell functions associated with cell proliferation, survival, and differentiation. Detailed T cell evaluation revealed normal total numbers of T lymphocytes including $CD4^+$ and $CD8^+$ cells and T follicular helper (T_{fH}) cells (fig. S2, C and D, and table S3) compared with published age-dependent reference values (*29*). However, subset analysis showed elevated relative percentages of central memory cells and exhausted effector memory cells (Fig. 2B and table S3). Furthermore, HEM1-deficient CD4 T helper memory subsets exhibited a hypersecretory

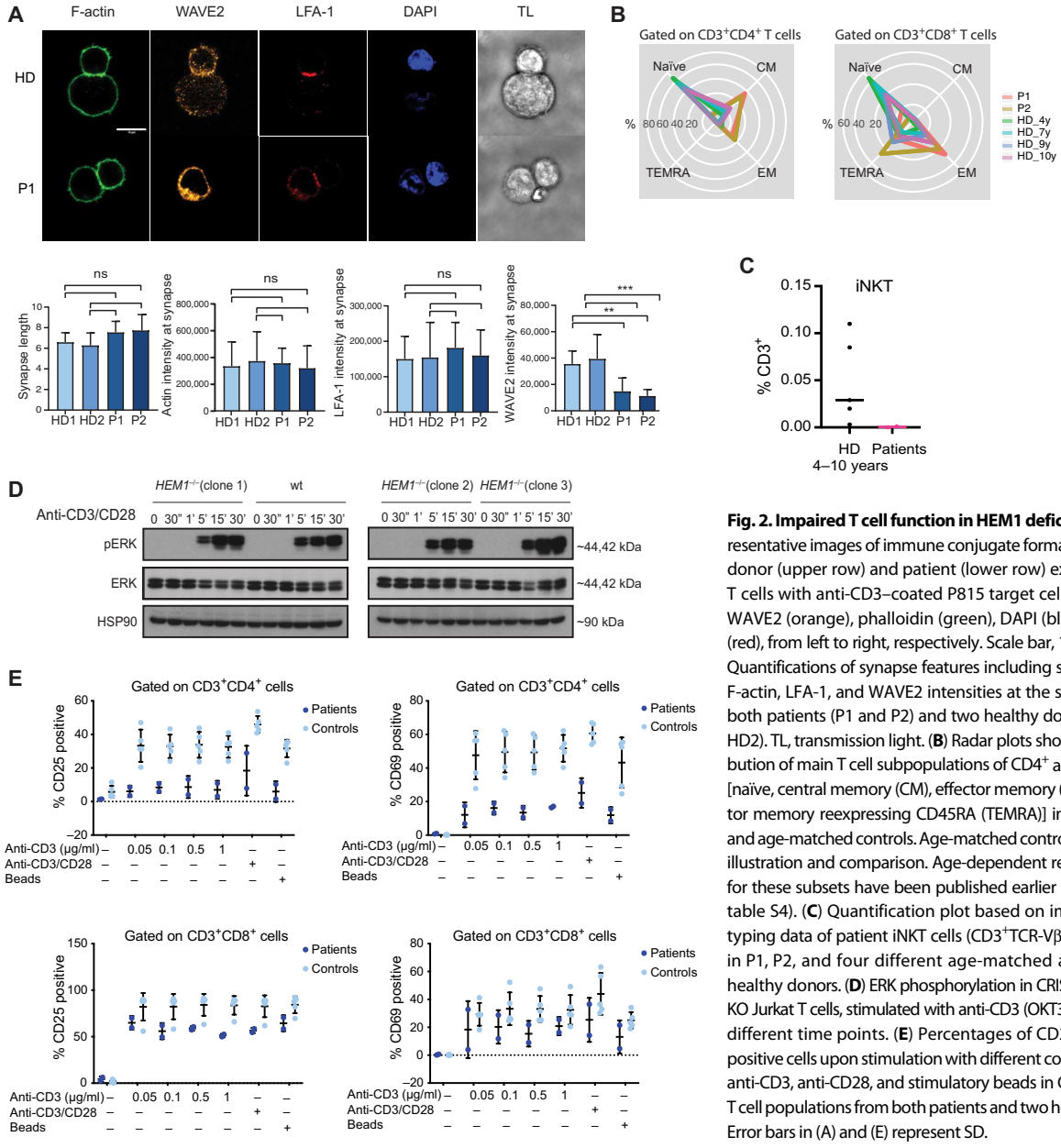

Fig. 2. Impaired T cell function in HEM1 deficiency. (**A**) Representative images of immune conjugate formation in healthy donor (upper row) and patient (lower row) expanded $CD8^+$ T cells with anti-CD3–coated P815 target cells stained with WAVE2 (orange), phalloidin (green), DAPI (blue), and LFA-1 (red), from left to right, respectively. Scale bar, 10 μm. Bottom: Quantifications of synapse features including synapse length, F-actin, LFA-1, and WAVE2 intensities at the synapse area in both patients (P1 and P2) and two healthy donors (HD1 and HD2). TL, transmission light. (**B**) Radar plots showing the distribution of main T cell subpopulations of $CD4^+$ and $CD8^+$ T cells [naïve, central memory (CM), effector memory (EM), and effector memory reexpressing CD45RA (TEMRA)] in both patients and age-matched controls. Age-matched controls are for easier illustration and comparison. Age-dependent reference values for these subsets have been published earlier (for details, see table S4). (**C**) Quantification plot based on immunophenotyping data of patient iNKT cells ($CD3^+$TCR-Vβ11$^+$,TCRVα24$^+$) in P1, P2, and four different age-matched and one adult healthy donors. (**D**) ERK phosphorylation in CRISPR-Cas9 *HEM1* KO Jurkat T cells, stimulated with anti-CD3 (OKT3)/anti-CD28 for different time points. (**E**) Percentages of CD25- and CD69-positive cells upon stimulation with different concentrations of anti-CD3, anti-CD28, and stimulatory beads in $CD4^+$ and $CD8^+$ T cell populations from both patients and two healthy controls. Error bars in (A) and (E) represent SD.

T helper 1 (T_H1)–biased phenotype compared with age-matched controls (fig. S2E). Invariant natural killer T (iNKT) cells were very low to absent in both patients (Fig. 2C), whereas the proportion of T cell receptor $\gamma\delta^+$ (TCR$\gamma\delta^+$) cells compared with TCR$\alpha\beta$ cells showed a relative increase within the $CD8^+$ T cell subset (table S3), both as seen in other immunodeficiencies with marked immune dysregulation (*30*). Patients had only slightly elevated double-negative T (DNT) cells compared with published age-dependent reference values (table S3) (*29*). Increased DNTs are characteristic of autoimmune lymphoproliferative syndrome (ALPS) (*31*). However, expression of fatty acid synthase (FAS), FAS ligand–mediated apoptosis (fig. S2F), and ALPS biomarkers were unremarkable, inconsistent with classical ALPS. Similarly, haploinsufficiency of the regulatory cytotoxic T lymphocyte antigen–4 (CTLA-4) is known to cause severe systemic autoimmunity and immunodeficiency (*32*). Nevertheless, we found that expression of PD-1/PD-L1 and cycling of the immune checkpoint CTLA-4 were unaffected (fig. S2, G and H), and no substantial reduction of regulatory T cell numbers was detected in the patients (table S3). We did, however, observe that both $CD4^+$ T cells and $CD8^+$ T cells were defective in antigen-induced proliferation independent of extracellular signal–regulated kinase (ERK) activation as observed in CRISPR–Cas9-engineered HEM1 KO jurkat T cells (Fig. 2D and fig. S2i) after stimulation with anti-CD3 and anti-CD28 antibodies. This phenotype was accompanied by impaired expression of the activation markers CD25 and CD69 (Fig. 2E).

Aberrant B cell phenotype in HEM1 deficiency

Loss of immune tolerance in SLE is supposedly multifactorial and includes a breakdown of T and B cell tolerance (*33*, *34*). The presence of autoantibodies despite normal total immunoglobulin G (IgG),

IgM, or IgA levels in P1 suggested aberrant B cell selection at the germinal center (GC) stage. Consistent with the observations in T cells, patient B cells also displayed decreased spreading and lack of lamellipodia upon IgM stimulation (Fig. 3, A and B, and table S4). These data suggested that, in addition to processes associated with antigen-induced proliferation of T cells, HEM1 deficiency might affect cell proliferation and/or differentiation in the B cell compartment. Therefore, we decided to evaluate patient B cell subsets. Absolute counts of $CD19^+$ cells and proportions of naïve, memory, and transitional B cells were within the aged-matched normal range compared with previously published data (*35*) (Fig. 3, C and D; fig. S3, A and B; and table S5), but patients showed an increase in cell subsets, such as innate-like $CD19^+CD38^{lo}CD21^{lo}$ ($CD21^{low}$) memory B cells, which were previously reported to be associated with autoimmunity (Fig. 3E) (*35*–*37*). $CD21^{low}$ memory-like B cells expand in conditions characterized by chronic immune stimulation (*38*), and studies using chronic infection models showed that activity of these cells is inversely correlated with BAFFR expression due to increased cleavage of BAFFR upon BAFF stimulation (*38*). Therefore, we decided to evaluate BAFF levels in patients' serum. However, surface measurements of BAFFR on HEM1-deficient patient B cell subsets revealed reduced levels of BAFFR on $CD19^+$ cells and B cell subsets, indicating constant activation of these cells (Fig. 3F).

$Hem1^{-/-}$ mice replicate aberrant B cell development and multifaceted autoimmunity

To gain a mechanistic understanding of how HEM1 deficiency affects B cell development and GC maturation, we took advantage of a recently generated $Hem1^{-/-}$ mouse model (fig. S4, A to C) (*25*). We found that $Hem1^{-/-}$ mice suffered from severe systemic autoimmunity manifesting in splenomegaly, immune complex/lupus glomerulonephritis with mesangial enlargement, hypercellularity, sclerosis (Fig. 4, A and B), and IgG and C3 deposits (Fig. 4B). Further, we detected massively increased levels of proinflammatory markers, including interleukin-6 (IL-6), interferon γ (IFNγ), and MRP8/14 (Fig. 4C), likely underlying the observed neutrophilia and monocytosis in the peripheral blood and the spleen (fig. S4, D and E) as well as granulomatous lesions in multiple organs (fig. S4F). We also found aberrant leukocyte development in the bone marrow (Fig. 4D) and extramedullary hematopoiesis in the spleen as previously described for $Hem1^{-/-}$ mice (fig. S4G) (*39*). Although T cell numbers were unaltered in the spleen (fig. S4H), $Hem1^{-/-}$ mice had an expansion of the memory T cell compartment, phenocopying the HEM1-deficient patients (Fig. 2B). Blood B cell counts were rather reduced (Fig. 4E), and mature recirculating follicular B cells were almost absent in both the periphery (Fig. 4F) and bone marrow (fig. S4I), resulting in an increased ratio of immature/mature B cells (Fig. 4F).

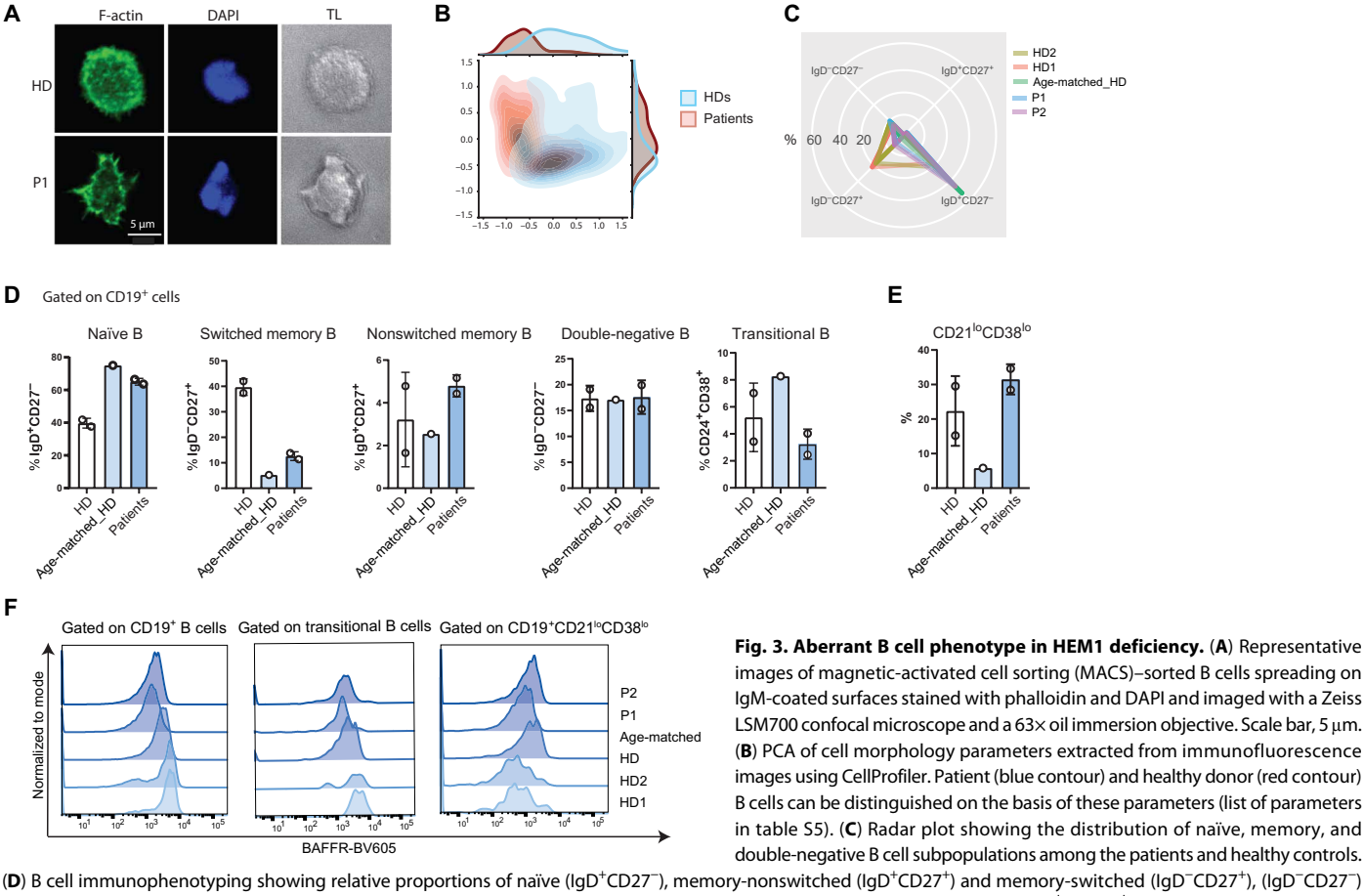

Fig. 3. Aberrant B cell phenotype in HEM1 deficiency. (**A**) Representative images of magnetic-activated cell sorting (MACS)–sorted B cells spreading on IgM-coated surfaces stained with phalloidin and DAPI and imaged with a Zeiss LSM700 confocal microscope and a 63× oil immersion objective. Scale bar, 5 µm. (**B**) PCA of cell morphology parameters extracted from immunofluorescence images using CellProfiler. Patient (blue contour) and healthy donor (red contour) B cells can be distinguished on the basis of these parameters (list of parameters in table S5). (**C**) Radar plot showing the distribution of naïve, memory, and double-negative B cell subpopulations among the patients and healthy controls. (**D**) B cell immunophenotyping showing relative proportions of naïve (IgD^+CD27^-), memory-nonswitched (IgD^+CD27^+) and memory-switched (IgD^-CD27^+), (IgD^-CD27^-) double-negative B cells, and relative proportions of transitional ($CD19^+CD24^+CD38^+$) and (**E**) memory-like ($CD19^+CD27^-IgD^+CD21^{low}CD38^{low}$) B cells (gating strategy as outlined in fig. S3A). Error bars in (D) and (E) represent SD. (**F**) Expression of BAFFR (BV605) on the surface of $CD19^+$, transitional, and $CD21^{low}CD38^{low}$ B cells of P1, P2, age-matched, and adult healthy donors (gating strategy as explained in fig. S3A).

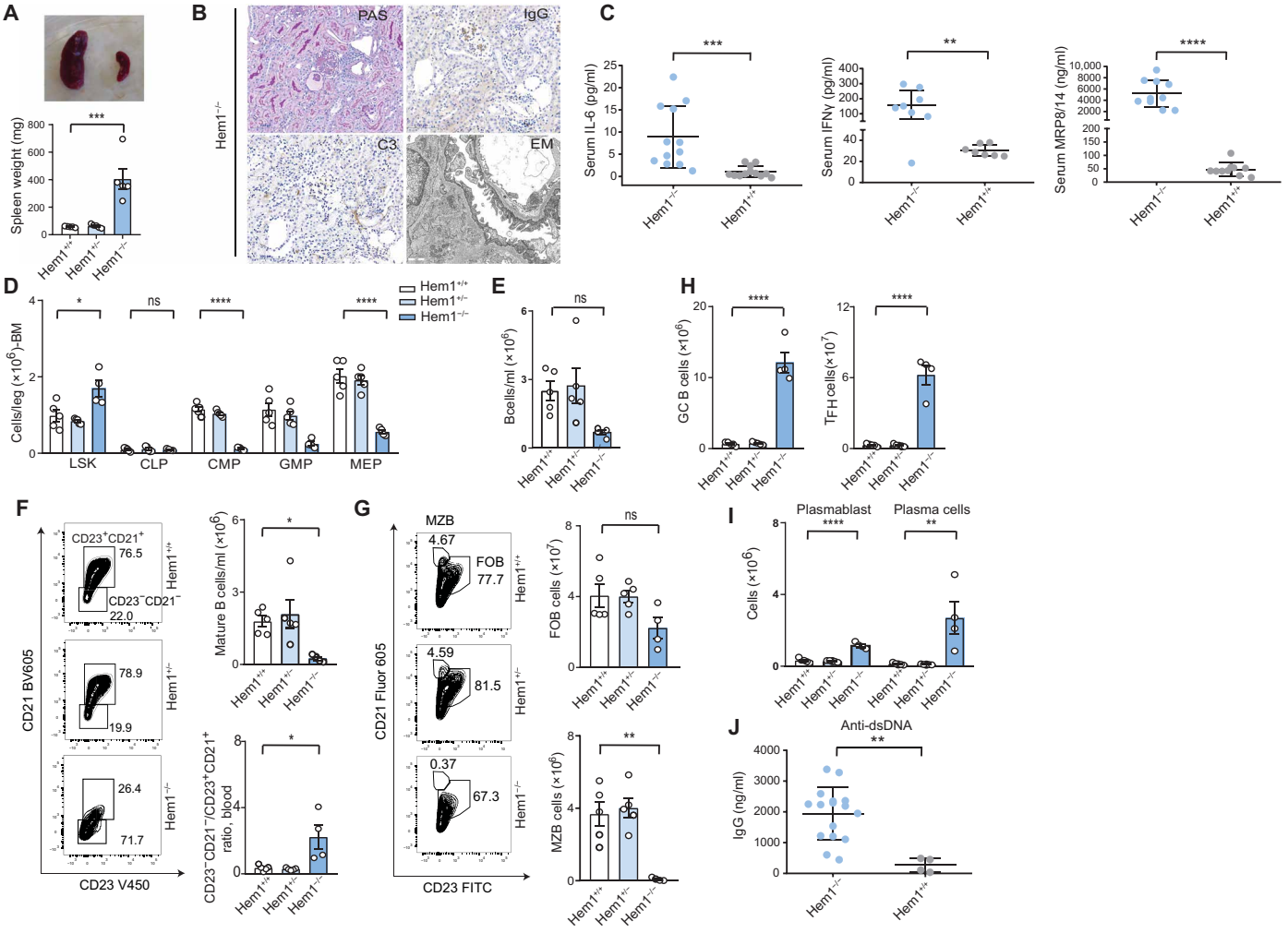

Fig. 4. Hem1$^{-/-}$ mice replicate aberrant B cell development and autoantibody generation. (**A**) Representative image and comparison of spleen size of the Hem1$^{-/-}$ versus Hem1$^{+/+}$ mice. (**B**) Immunohistochemistry and electron microscopy of kidneys from Hem1$^{-/-}$ mice illustrating severe systemic autoimmunity by glomerulonephritis (mesangial enlargement, hypercellularity and sclerosis, and C3 deposits). (**C**) IL-6, IFNγ, and MRP8/14 cytokine levels in wt (Hem1$^{+/+}$) and KO (Hem1$^{-/-}$) mice. Each dot represents one mouse. (**D**) LSK (Lin^{-}Sca1^{+}Kit^{-}) stem cells in the bone marrow (BM) of Hem1$^{+/+}$, Hem1$^{+/-}$ (heterozygous), or Hem1$^{-/-}$ mice. (**E**) Quantification of total blood B cells (B220). (**F**) Quantification of mature blood B cells (CD21^{+}CD23^{+}) (top, right) and ratio of mature (CD21^{+}CD23^{+}) and immature B cells (CD21low CD23^{-}) of Hem1$^{+/+}$, Hem1$^{+/-}$, or Hem1$^{-/-}$ mice in blood (bottom, right); representative fluorescence-activated cell sorting (FACS) plots (left). (**G**) Representative flow cytometry plots of marginal zone (MZB) (B220^{+}CD21^{hi}CD23^{-}) and follicular (FOB) (B220^{+}CD21^{int}CD23^{+}) B cells in the spleen of Hem1$^{+/+}$, Hem1$^{+/-}$, or Hem1$^{-/-}$ mice (left) and quantification (right). (**H**) Representative flow cytometry quantification of splenic GL-7^{hi} GC B cells in Hem1$^{+/+}$, Hem1$^{+/-}$, or Hem1$^{-/-}$ mice. Representative flow cytometry quantification of T_{fH} cells (CD3^{+}CD4^{+}PD1^{+}CXCR5^{+}). (**I**) Quantification of representative flow cytometry plots along with the enumeration of splenic plasmablast (CD138^{+},B220^{+}) and plasma cell (CD138^{+}B220^{-}) counts in Hem1$^{+/+}$, Hem1$^{+/-}$, or Hem1$^{-/-}$ mice. (**J**) Anti-dsDNA–specific serum IgG titers of Hem1$^{+/+}$ and Hem1$^{-/-}$ mice quantified by enzyme-linked immunosorbent assay (ELISA). FITC, fluorescein isothiocyanate; CLP, common lymphoid progenitor; CMP, common myeloid progenitor; MEP, megakaryocyte-erythroid progenitor; GMP, granulocyte-macrophage progenitor. Error bars represent SEM in bar graphs and SD in (C) and (J).

Intriguingly, total splenic B cell numbers were unaltered (fig. S4J). In the spleen, Hem1$^{-/-}$ mice accumulated immature and transitional B cells, gated using IgD, CD19, and CD93, as previously described (*40*) (fig. S4K), and showed almost undetectable marginal zone and decreased follicular and mature B cells (Fig. 4G), explaining the lack of recirculating B cells (Fig. 4E). Numbers of both GL-7^{hi} GC B cells and PD-1^{+} T_{fH} cells (Fig. 4H) were drastically elevated in Hem1-deficient mice. Consistent with findings in HEM1-deficient individuals, Hem1$^{-/-}$ mice produced manifold more potentially autoreactive antibody-secreting plasmablasts (Fig. 4I) and showed accumulation of serum dsDNA autoantibodies as early as 3 to 4 weeks of age (Fig. 4J), similar to findings in HEM1-deficient patients. In sum, these data suggest that the B cell compartment undergoes substantial changes in response to Hem1 deficiency in mice.

Single-cell RNA sequencing uncovers dysregulated B cell development

To investigate the dynamics of these changes in a systematic fashion, we decided to characterize splenic cell subsets via 10× single-cell RNA sequencing (RNA-seq) in total homogenized erythrocyte-depleted spleen suspension of 5- and 10-week-old Hem1$^{+/+}$ and Hem1$^{-/-}$ mice. We were able to resolve the main leukocyte subsets using the Leiden clustering algorithm (Fig. 5, A and B). To identify hotspots of clustering, we evaluated cellular density and found three

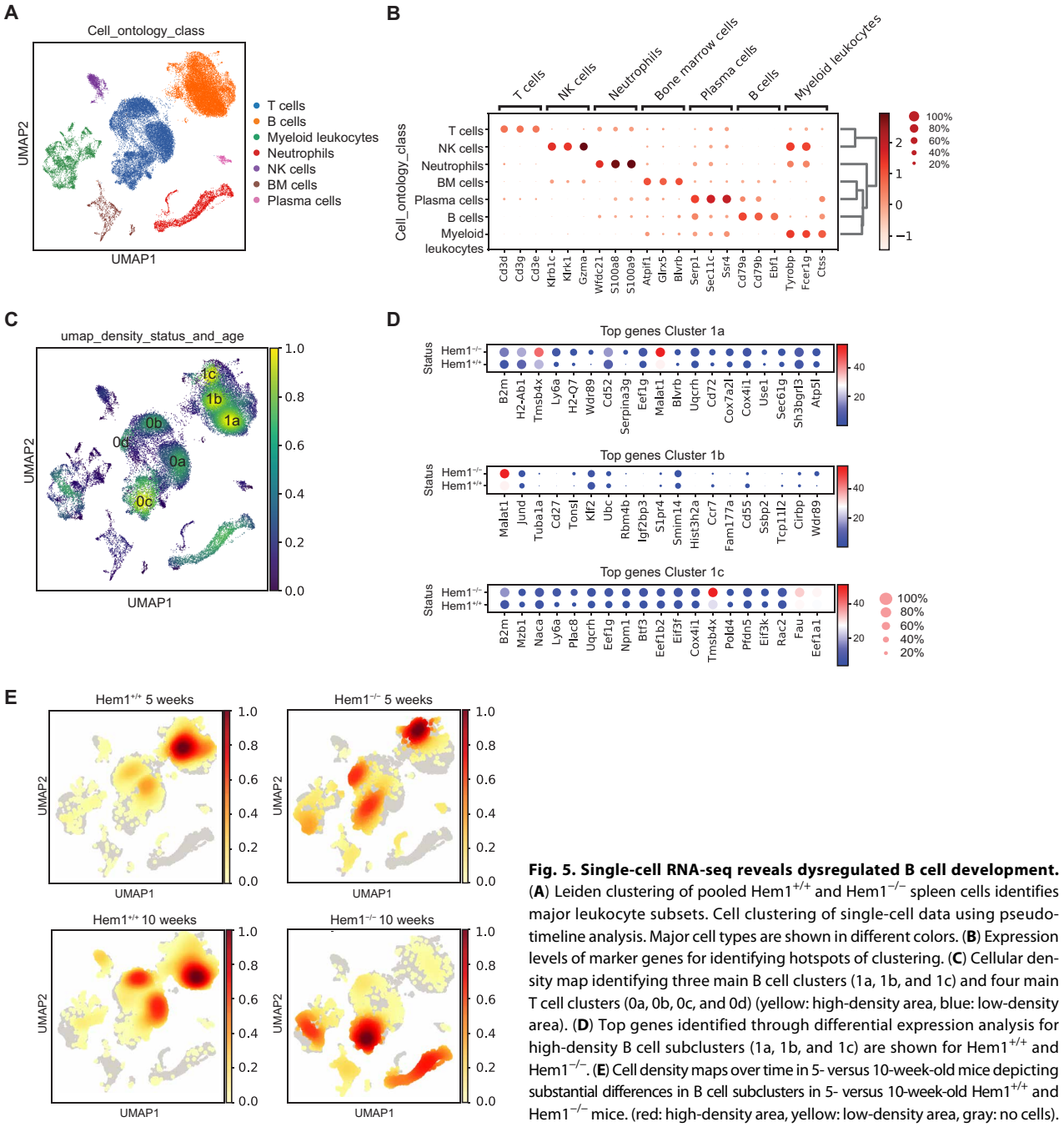

Fig. 5. Single-cell RNA-seq reveals dysregulated B cell development. (**A**) Leiden clustering of pooled Hem1$^{+/+}$ and Hem1$^{-/-}$ spleen cells identifies major leukocyte subsets. Cell clustering of single-cell data using pseudotimeline analysis. Major cell types are shown in different colors. (**B**) Expression levels of marker genes for identifying hotspots of clustering. (**C**) Cellular density map identifying three main B cell clusters (1a, 1b, and 1c) and four main T cell clusters (0a, 0b, 0c, and 0d) (yellow: high-density area, blue: low-density area). (**D**) Top genes identified through differential expression analysis for high-density B cell subclusters (1a, 1b, and 1c) are shown for Hem1$^{+/+}$ and Hem1$^{-/-}$. (**E**) Cell density maps over time in 5- versus 10-week-old mice depicting substantial differences in B cell subclusters in 5- versus 10-week-old Hem1$^{+/+}$ and Hem1$^{-/-}$ mice. (red: high-density area, yellow: low-density area, gray: no cells).

main B cell (1a, 1b, and 1c) and four main T cell clusters (0a, 0b, 0c, and 0d) (Fig. 5C; fig. S5, A and B; and tables S6 and S7). On the basis of the differential expression analysis of B cell subclusters, we attributed cluster 1a to follicular B cells and 1b to GC B cells present in wt conditions. However, cluster 1c mainly present in the Hem1$^{-/-}$ situation could not be attributed to a specific stage of B cell development (Fig. 5D). We speculated that this cluster may emerge from dysregulation of the B cell developmental program in the absence of Hem1. Evaluation of cell density maps over time revealed substantial differences in B cell subclusters in 5- versus 10-week-old mice, suggesting a disturbed B cell developmental program that consequently leads to alterations in T cell subsets (Fig. 5E). Whereas in Hem1$^{+/+}$ mice most B cells shifted from the GC cluster (1b) to the follicular B cell cluster (1a), Hem1$^{-/-}$ mice showed the highest density in cluster 1c at 5 weeks but a global reduction in total B cells at 10 weeks, indicating a substantial loss of splenic B cells (Fig. 5E). Furthermore, we observed that T cell clusters also show aberrant differentiation in Hem1$^{-/-}$ versus Hem1$^{+/+}$ mice calculated using entropy analyses (*41*, *42*) (fig. S5C), further extending findings from an early study in an ENU (*N*-ethyl-*N*-nitrosourea)–mutant mouse model (*43*).

Defective B cell–intrinsic survival in murine Hem1$^{-/-}$ B cells

Considering the aberrations in both T and B cell subclusters, we wanted to determine whether there is a B cell–intrinsic defect in the

context of Hem1 deficiency. For this purpose, we made use of the J_HT mouse strain (*44*). J_HT mice harbor a deletion of the J_H minigenes generated through the Cre-loxP system and are truly devoid of B cells and Igs in all tested genetic backgrounds. The non–B cell compartment in J_HT mice cannot be considered mixed, but is predominantly wt, and therefore, non–B cells are fully functional using this approach (*45*). We generated bone marrow chimeras of J_HT and $Hem1^{-/-}$ versus $Hem1^{+/+}$ bone marrow, in a ratio of 80% (J_HT bone marrow) to 20% (either $Hem1^{+/+}$ or $Hem1^{-/-}$ bone marrow), and transplanted them into sublethally irradiated C57BL/6J mice (referred to as J_HT $Hem1^{+/+}$ and J_HT $Hem1^{-/-}$ bone marrow; Fig. 6A). In recent work, Shao *et al.* (*38*) demonstrated that Hem1-deficient hematopoietic stem cells may fail to engraft the bone marrow. To control for a potential engraftment issue, we also generated sublethally irradiated C57BL/6J mice transplanted with either $Hem1^{+/+}$ or $Hem1^{-/-}$ bone marrow alone (referred to as C57BL/6J $Hem1^{+/+}$ and C57BL/6J $Hem1^{-/-}$) and monitored all mice during a recovery period. Whereas as expected control C57BL/6J $Hem1^{-/-}$ mice fell severely ill and showed similar disease as seen in full-body $Hem1^{-/-}$ mice, C57BL/6J $Hem1^{+/+}$ mice remained healthy. J_HT $Hem1^{+/+}$ mice appeared healthy as well, whereas one J_HT-$Hem1^{-/-}$ mouse died and additional three mice showed considerable weight loss (Fig. 6, B and C), forcing us to terminate the experiment. Although reconstitution of hematopoietic cells was successful, as judged by the comparable numbers of stem cells $Lin^-Sca1^+Kit^-$ bone marrow cells (LSKs) in both groups (Fig. 6D), J_HT-$Hem1^{-/-}$ mice displayed a reduction in immature and, even to a greater extent, mature B cell numbers in the bone marrow (Fig. 6E). Moreover, in the context of this bone marrow transplantation strategy, B cell–specific Hem1 deficiency even resulted in the absence of detectable B cells both in peripheral blood (Fig. 6F), accompanied by increased numbers of circulating monocytes and neutrophils (Fig. 6G). As in other diseases, clinical phenotypes are complex and may originate from the interplay of different cell populations; however, these experiments indicate a critical role of HEM1 deficiency on B cell homeostasis and hence a role for B cells in disease pathogenesis. In support, depmap analysis showed that the gene expression profiles of $Hem1^{-/-}$ B cells are unexpectedly similar to those in B cells deficient of Pax5 (*46*) or Irf8 (*47*), well-known master regulators of B cell development (fig. S6A).

Our findings prompted us to further investigate how a cytoskeletal protein such as HEM1 may influence B cell development. To this end, we first performed differential gene expression and pathway enrichment analyses in B cells. We found antigen presentation, leukocyte differentiation, and cell adhesion as the most enriched pathways in $Hem1^{-/-}$ compared with $Hem1^{+/+}$ B cells (tables S8 and S9). Because all these cellular pathways ensure the development of normal, non-autoreactive B cells, we decided to examine whether patient B cells display any abnormalities associated with cell spreading and interactions with antigens. We found that patient B cells were unable to spread, as evidenced from a significantly decreased cell spreading area on ligand-coated substrates (Figs. 3, A and B, and 7A and fig. S6B). Instead of assembling polarized lamellipodia and membrane ruffles, cells assumed a rather rounded blebbing or spiky morphology normally associated with high levels of cortical actomyosin tension and the formation of long linear F-actin assemblies (fig. S6C). As a result of the decreased cell spreading, B cells exhibited a reduced capacity to recruit IgM and displayed a disorganized B cell immunological synapse (IS) required to efficiently engage and properly organize IgM molecules within the IS (Fig. 7, B and C, and fig. S6, B and D). This phenotype is specific to HEM1 deficiency and was not observed to a similar extent in WASP-deficient B cells (fig. S6E).

Because actin cytoskeleton–mediated organization of the B cell synapse is key to integrate stimulatory cues and activate downstream signaling pathways (*48*), we hypothesized that in the absence of HEM1, B cells fail to activate critical signaling cascades to a degree sufficient to maintain cell fitness and proper development. Such signaling cascades classically include the kinases ERK and phosphatidylinositol 3-kinase (PI3K), ultimately activating AKT, whose functions are critical to skew the balance of cell fate choices toward growth and proliferation. Hence, when we biochemically probed the activation status of the kinase AKT, we found a significant decrease in the amount of phosphorylated AKT (pAKT Ser^{473}) in patient cells compared with normal donor B cells (Fig. 7D). To execute its cell fate–controlling function, AKT operates through transcriptional regulators such as the evolutionarily conserved Daf-16–related Forkhead O (Foxo) family. Phosphorylation of the Foxo proteins by AKT is established to induce their nuclear export and subsequent inactivation of transcriptional activity indispensable for B cell development. Thus, we used nuclear levels of Foxo proteins as a readout of its transcriptional activity (*49*, *50*). We found that IgM-stimulated normal donor–derived B cells display significantly decreased nuclear levels of Foxo1 (Fig. 7E). By contrast, patient cells retained Foxo1 in the nucleus upon IgM stimulation, indicating that the AKT-mediated control of Foxo1 nuclear-cytoplasmic shuttling and thus transcriptional activity is attenuated in HEM1-deficient B cells (Fig. 7E) (*50*).

Foxo1 also operates as a transcriptional repressor of genes promoting B cell survival, proliferation, and proper differentiation. Consistent with the above-described accumulation of Foxo1 in the nucleus of patient HEM1-deficient B cells, our analysis of single-cell RNA-seq data in mouse splenic B cells revealed Foxo1 targets (*51*) among top transcriptionally deregulated genes in $Hem1^{-/-}$ versus $Hem1^{+/+}$ B cells. For instance, we found that pro-proliferative genes (*Myc*, *Cdkn1b*, *Cdk1*, and *Rbl2*), normally repressed by Foxo1, were reduced (Fig. 7F), whereas genes promoting controlled DNA damage (*Ddb1*) and controlling apoptosis (*Fas*, *Bcl2*, *Bcl6*, and *Batf*) via transcriptional activation by Foxo1 were up-regulated in $Hem1^{-/-}$ B cells (Fig. 7F and fig. S6F). This transcriptional pattern was most evident in cluster 1c (Fig. 5D) that did not appear to correspond to any specific stage of B cell development. Therefore, we concluded that this cell cluster most probably emerges from the dysregulation of B cell developmental program resulting from Hem1 deficiency.

DISCUSSION

The multicomponent WRC is traditionally considered as one of the key molecular machineries enabling actin-driven migration of a variety of animal tissue cell types (*7*, *10*, *26*). More recent studies of the WRC in immune cell migration reveal that its subunits are not necessarily essential for basal cell migration but mainly contribute to the ability of rapidly crawling amoeboid leukocytes to navigate extracellular spaces with increasing geometrical complexity (*25*). Given the conditional nature of the role of the WRC in cell migration and the systemic severity of KO phenotypes for WRC subunits (e.g., Wave2) at an organismal level (*10*), it is unlikely that WRC has evolved to regulate cell locomotion only. Here, by dissecting the pathobiology underlying a previously unknown inborn error of human immunity caused by deficiency in the hematopoietic-specific

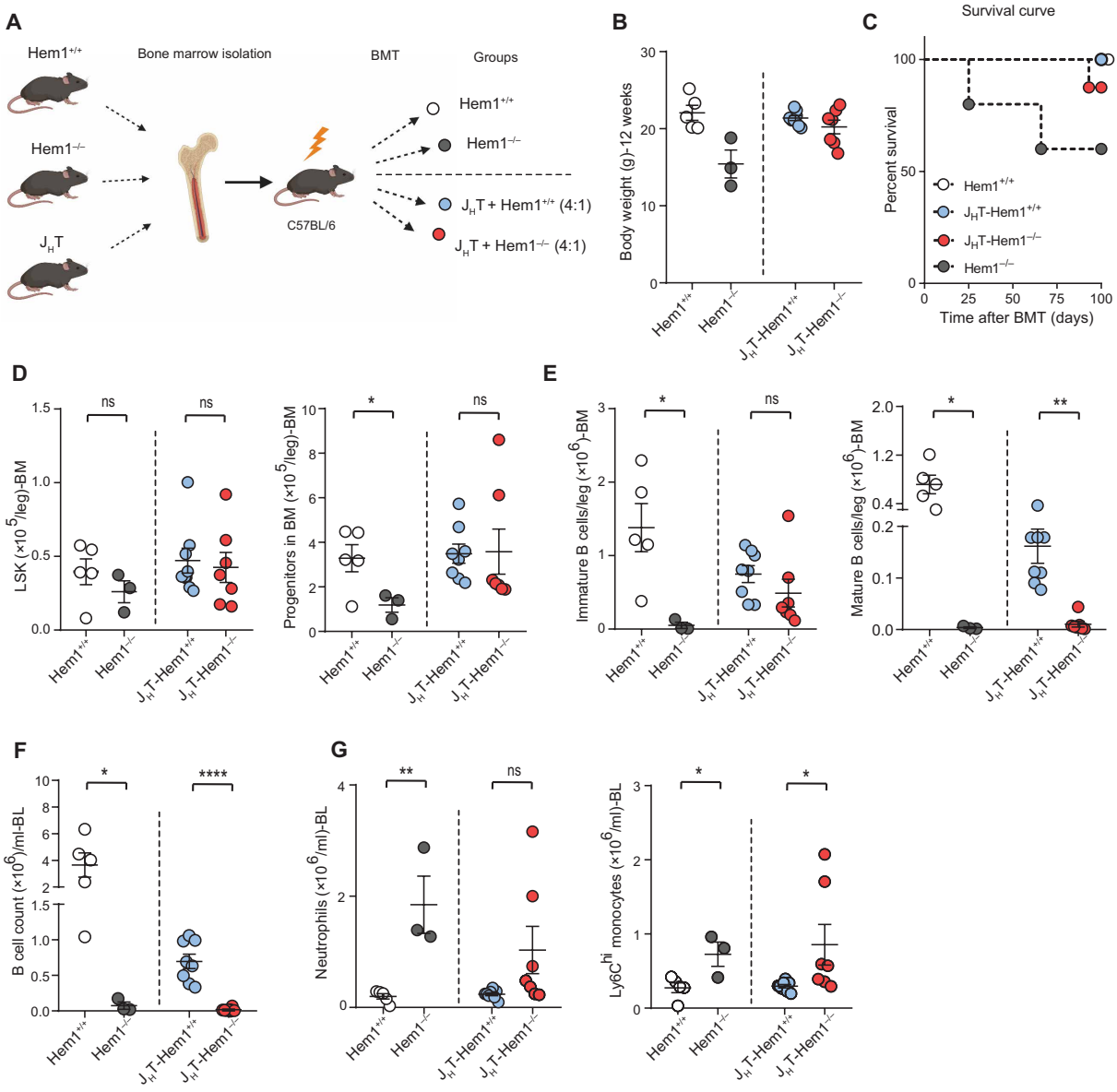

Fig. 6. Defective B cell–intrinsic survival in murine Hem1$^{-/-}$ B cells. (**A**) Scheme for the transplantation experiment: Mixed bone marrow chimeras of J_HT and Hem1$^{-/-}$ versus Hem1$^{+/+}$ bone marrow were transplanted into sublethally irradiated Bl6 mice (Hem1$^{+/+}$). Control groups consisted of mice receiving Hem1$^{+/+}$ or Hem1$^{-/-}$ bone marrow (shown in white and gray dots). The four transplanted groups are depicted in the figure. (**B**) Body weight of the four different groups of transplanted mice at the termination point of experiment (12 weeks). (**C**) Kaplan-Meier survival curve of bone marrow chimera experiment [C57BL/6J mice with mixed J_HT and wt bone marrow (4:1) and C57BL/6J mice with mixed J_HT and KO bone marrow (4:1)]. (**D**) Absolute number of LSK (left) and progenitor cells (right) in transplanted mice with J_HT-Hem1$^{+/+}$ and J_HT-Hem1$^{-/-}$ chimeras and control groups. (**E**) Absolute number of immature (left) and mature (right) B cells in the bone marrow of transplanted mice. (**F**) Absolute number of blood B220$^+$ B cells in transplanted mice with J_HT-Hem1$^{+/+}$ and J_HT-Hem1$^{-/-}$ chimeras and the control groups. (**G**) Absolute number of neutrophils in blood of transplanted mice with J_HT-Hem1$^{+/+}$ and J_HT-Hem1$^{-/-}$ chimeras and the control groups (left). Absolute number of blood Ly6C^{hi} monocytes of J_HT-Hem1$^{+/+}$ and J_HT-Hem1$^{-/-}$ chimeras and the control groups (right). BMT, bone marrow transplantation.

WRC component HEM1, we uncover a role for the WRC in the context of B cell development and homeostasis (Fig. 7G).

Over the past years with the discoveries of key regulators of immune homeostasis, it became clear that there is considerable variability, as the clinical presentation of even patients with the same genetic disorder may vary from subclinical to severe systemic autoimmunity, as exemplified in patients with germline mutations in *PIK3CD*, *CTLA4*, or *DEF6* (*32*, *52*, *53*). Reminiscent of such observations, we detected phenotypic variability in HEM1-deficient individuals, with the more severely affected patient P1 showing an SLE-like autoimmune disease phenocopied by a Hem1-deficient mouse model, whereas the clinical phenotype of P2, to date, has remained milder despite similar B cell phenotypic aberrations including increased CD21^{lo}CD38^{lo} B cells. Aberrant B cell phenotypes similar to our observations for HEM1 deficiency are seen in other SLE and Common Variable Immunodeficiency (CVID) patients, including reduced

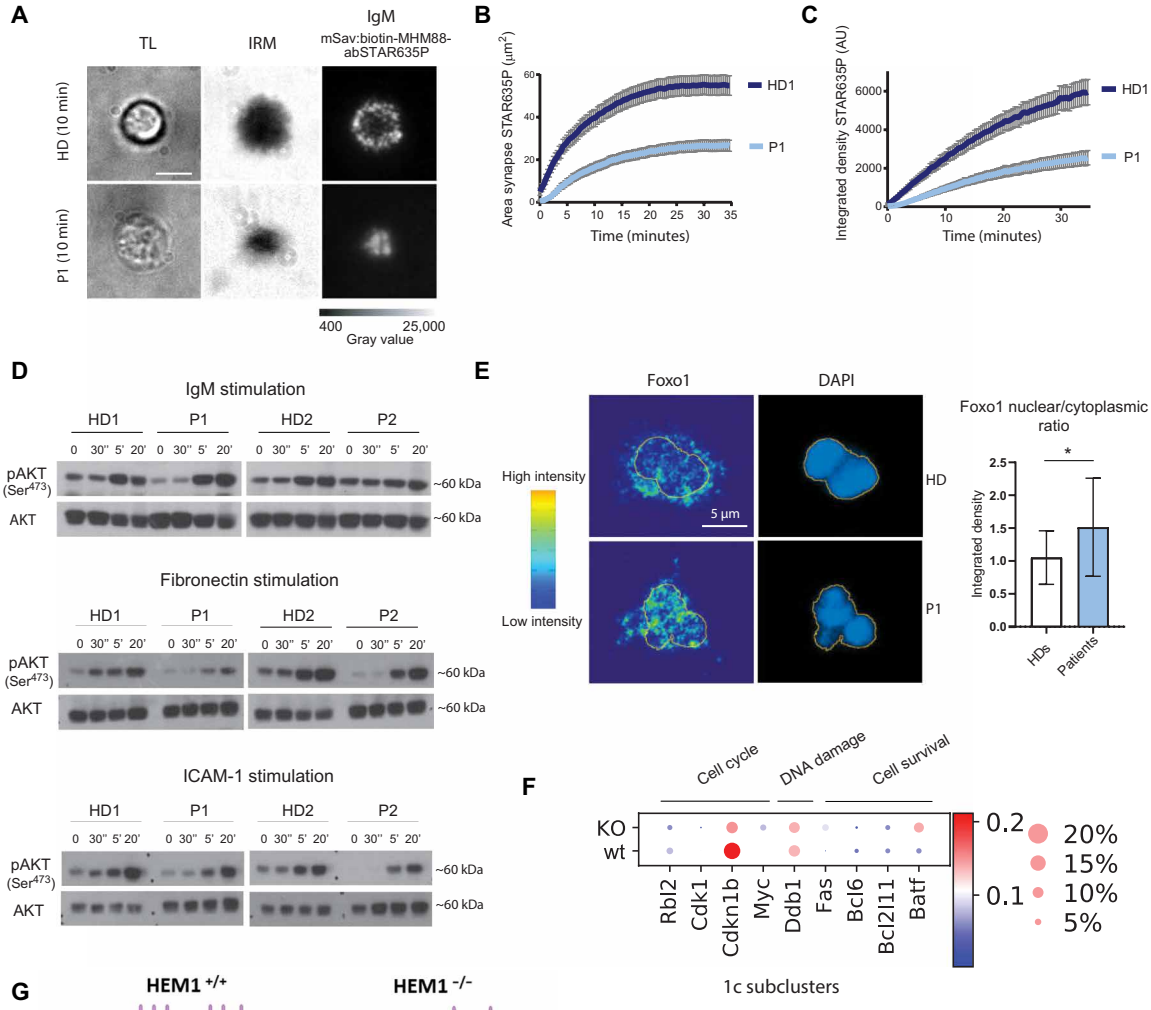

Fig. 7. Disrupted BCR signaling in HEM1 deficiency. (**A**) Healthy donor (top) and patient (bottom) B cells after IgM stimulation using a planar-supported lipid bilayer functionalized with a monovalent streptavidin platform presenting biotinylated and abSTAR635P-conjugated MHM88 monoclonal antibodies, TL (left), interference reflection microscopy (IRM) (middle), and IgM (right). Scale bar, 5 μm. (**B**) Area of IgM (abSTAR635P)/μm^2 over time illustrates accumulation of IgM at the IS. (**C**) Integrated density of IgM [arbitrary units (AU)] over time illustrates intensity of IgM at the IS (HD1, dark blue; patient 1, light blue) (**D**) Representative EBV-LCL–transformed B cell Western blots of P1, P2, and two healthy donors of pAKT (Ser^{473}) and total AKT including ratios of phosphorylated/total AKT by IgM, fibronectin, and ICAM-1 stimulation. (**E**) Immunofluorescence staining of patient- and healthy donor–derived primary B cells for Foxo1 and DAPI after IgM stimulation illustrating increased levels of Foxo1 in the nucleus of P1. Quantification of nuclear/cytoplasmic ratio of both P1 and P2 (pooled) and two healthy donors. The yellow line indicates the nuclear border, intensity map (left). Error bars represent SD. (**F**) Representative graphs for *Foxo1* target genes regulating cell cycle progression (*Rbl2*, *Cdk1*, *Cdkn1b*, and *Myc*), DNA damage (*Ddb1*), and apoptosis (*Bcl6*, *Bcl2l11*, and *Batf*). (**G**) Scheme illustrating proposed mechanism.

switched memory B cells and expanded CD21^{lo}CD38^{lo} B cells. Although clonally related to memory B cells and plasmablasts, these cells form distinct clades within phylogenetic trees based on accumulated variable gene mutations, supporting exit from active GCs (*37*). CD21^{lo}CD38^{lo} B cells express a transcriptional program, suggesting that they are primed for plasma cell differentiation and are refractory to GC differentiation (*37*). During GC maturation, B cells repetitively test and adapt their BCR to ensure the development of a tolerant, non-autoreactive BCR (*54*). B cells constantly take up soluble antigens predominantly via clathrin-coated pits (*55*), but uptake of cell-bound antigens requires additional, larger-scale processes involving F-actin–mediated cell shape reorganization. Encountering antigen-presenting

cells (APCs) bearing cognate antigen, B cells begin establishing the immune synapse (IS) (*56*) by spreading across the surface of the APC to scan for additional antigens. This process is followed by membrane contraction and the formation of antigen receptor microclusters initiating the signaling reactions necessary for lymphocyte activation (*47*).

We found that in the absence of HEM1, B cells fail to spread properly and exhibit a lower coverage of antigen-presented surfaces due to the lack of lamellipodia. This, in turn, results in significantly less efficient aggregation of membrane bilayer–bound IgM molecules within the B cell IS. These morphodynamic aberrations in B cell IS formation and function decrease the strength of the extracellular signal required to tune BCR signaling toward normal B cell development. We hypothesize that in HEM1-deficient GCs, the control of developmental and survival programs is hijacked by autoreactive antigens as they elicit stronger signals, shifting the balance of B cell fate choices toward survival of autoreactive B cells and the development of autoimmunity. Similar defects in T cell IS formation may further promote the disease progression, as cognate interactions between T and B lymphocytes lead to a bidirectional signal exchange (*28*, *47*, *55*). In addition, we speculate that when HEM1-deficient B cells extract antigens from live APCs, lack of Arp2/3-mediated actin branching reduces membrane flexibility hindering BCR-dependent membrane invagination and, as a result, antigen extraction. At the same time, formins known to take over the actin polymerase activity in the absence of Arp2/3-mediated actin branching would promote unbranched linear actin filament generation, which can sterically impede dynamic signal extraction. Collectively, these processes explain a reduced amount of perceived cell-bound signal.

Mutations in genes encoding multiple actin cytoskeleton regulators have now been characterized as causing distinct inborn error of immunity (IEI) entities (*57*). In addition to combined impairments in innate and adaptive immunity, autoimmunity emerges as a common feature of some actin-associated IEIs. Studies in the prototypical Wiskott-Aldrich syndrome have highlighted the pivotal role of the Arp2/3 activator WASP in controlling BCR and Toll-like receptor signaling in a B cell differentiation stage–dependent manner, with elevated responsiveness in immature B cells and reduced responsiveness in mature B cells (*58*, *59*). Compared with WASP deficiency, DOCK8 deficiency is associated to accumulation of autoreactive B cells (*60*). As suggested by studies in murine models, WIP deficiency, still poorly investigated in humans, might also be associated with autoimmunity due to aberrant B cell activation (*61*). In parallel to WAVE, also WASP, DOCK8, and WIP, which have been shown to interact (*62*), control actin branching via the ARP2/3 complex. The overlapping function of these proteins in tuning B cell activation and tolerance may therefore be due to the fact that they converge in controlling spatiotemporal activation of the ARP2/3 complex. A recent study showed that pharmacological inhibition of ARP2/3 impairs BCR microcluster mobility, promoting APC-induced B cell activation at the IS (*63*). Our study highlights that beyond these overlapping aspects, the WAVE versus WASP-mediated activation of Arp2/3 in B cells may differ, in terms of both molecular control and associated phenotype.

Collectively, we here characterize a loss-of-function mutation in WRC actin regulatory complex, which results in B cell developmental dysregulation and autoimmunity. We demonstrate that the WRC critically regulates extracellular signal perception and signal bridging, identifying a major and previously unrecognized role for the WRC in B cell development and immune homeostasis across species.

MATERIALS AND METHODS

Study design

The objective of this study was to investigate the role of HEM1 in human and mouse immune system and the consequence of HEM1 deficiency in immune dysregulation and autoimmunity. For this purpose, we made use of primary material from two HEM1-deficient patients, which were genetically analyzed in our laboratory primarily, and also, we used Hem1$^{-/-}$ mouse as an animal model. To study the cellular functions in this genetic defect, we also produced cell line models, which are described in the following sections.

Patients and ethics

Patients and other family member samples were included after collecting informed written consent and with approval from the ethics committee of the Tehran University of Medical Sciences. The patients were evaluated, followed up, and treated at the Departments of Rheumatology and Immunology at Children's Medical Center Hospital, Tehran University of Medical Sciences, Tehran, Iran. The study was approved by the local ethics committee of the Medical University of Vienna, Austria.

Animal experiments ethics

All experimental studies were approved by the Animal Ethics Committee of the Medical University of Vienna, Austria and were performed according to the guidelines for Good Scientific Practice of the Medical University of Vienna, Austria.

Exome sequencing

For ES, a TrueSeq Rapid Exome kit as well as the Illumina HiSeq3000 system and the cBot cluster generation instruments were used as previously described (*64*, *65*), with minor changes. Briefly, reads were aligned to the human genome version 19 by means of the Burrows-Wheeler Aligner (BWA). VEP (variants effect predictor) was used for annotating single-nucleotide variants and insertions/deletions lists. The obtained list was then filtered according to the presence of variants with a minor allele frequency (MAF) of >0.01 in 1000 Genomes, gnomAD, and dbSNP build 149. After further filtering steps for nonsense, missense, and splice-site variants using VCF.Filter software (*66*), an internal database was used to filter for recurrent variants. Moreover, variants are prioritized using tools, such as SIFT, Polyphen-2, and the CADD score as well as HGCS, that predict the deleteriousness of a present variant.

Preprocessing and analysis of single-cell RNA-seq data

For details regarding sample preparation, please see Supplementary Materials and Methods. Preprocessing of the single-cell RNA-seq data was performed using Single-Cell Software Suite (version 3.0.2, 10× Genomics) (*67*). Raw sequencing files were demultiplexed using the Cell Ranger command "mkfastq." Each sample was aligned to the human reference genome assembly "refdata-cellranger-mm10-1.2.0" using the Cell Ranger command "count," and all samples were aggregated using the Cell Ranger command "aggr" without depth normalization. Raw expression data were then loaded into Python 3.7.3 and analyzed using the Scanpy (1.4.5.post1) package (*68*).

Filtering and preparation of single-cell RNA-seq data

Cells with fewer than 700 detected genes, with fewer than 1200 counts, or that exceeded a total mitochondrial gene expression of 20% were removed. Genes expressed in fewer than 20 cells or fewer than three

counts were also removed. Count data were normalized (excluding highly expressed genes) and batch effect–corrected, and unwanted variations [number of counts per UMI (unique molecular identifier), mitochondrial fraction, and ribosomal fraction] were regressed out.

Clustering, differential expression, and further analyses

Highly variable genes (4000) were identified using the Cell Ranger (*67*) implementation in Scanpy (Single-Cell Analysis in Python) (*68*). Dimensionality reduction was performed using uniform manifold approximation and projection (UMAP) (*69*) and PCA. The PCA was based on the identified variable genes and limited to the first 50 principal components. The neighborhood graph was computed taking the UMAP and PCA into account. The Leiden (*70*) algorithm with a resolution of 0.1 grouped cells into clusters. By quantifying the connectivity of partitions with partition-based graph abstraction (*71*), the UMAP was recalculated and subclusters within the B cell and T cell identified using the Leiden algorithm with a resolution of 0.6 and 0.4, respectively. Differential expression analysis was performed based on *t* test, which overestimates variance of each group. The *P* values were adjusted for multiple testing using the Benjamini-Hochberg correction. Entropy analysis was performed using the SLICE (*72*) package following the standard workflow.

Data availability

All single-cell RNA-seq data included in this manuscript have been deposited with the functional genomics data store ArrayExpress (*73*) archive and accessible under the accession number E-MTAB-8706.

Flow cytometry analyses

All flow cytometric analyses were recorded on BD LSRFortessa. All data were analyzed using FlowJo X (TreeStar), and data were graphed with Prism 8.0 (GraphPad Software). For detailed experimental procedures and antibodies, see the Supplementary Materials.

Cell line generation and editing

For details regarding Jurkat, B16-F1 EBV-LCL generation and editing, as well as feeder T cell expansion, see the Supplementary Materials.

Rescue experiments and microscopy

Cells were transfected as described above and seeded on the following day onto 15-mm-diameter glass coverslips coated with laminin (25 μg/ml; Sigma-Aldrich, L2020) in laminin-coating buffer: 50 mM tris, 150 mM NaCl. Cells were allowed to adhere overnight and then fixed with prewarmed 4% paraformaldehyde (PFA; Sigma-Aldrich P6148) in phosphate-buffered saline (PBS) for 20 min. Permeabilization was carried out using 0.05% Triton X-100 in PBS for 1 min, subsequently followed by three washing steps with 1× PBS. To visualize the actin cytoskeleton, cells were subjected to phalloidin staining (ATTO-594–conjugated phalloidin, ATTO-TEC AD594-81, 1:200) and finally mounted onto glass slides using ProLong Gold antifade reagent (Thermo Fisher Scientific, P36934). PFA-fixed samples of cells expressing certain EGFP-tagged proteins of interest were analyzed on an inverted microscope (Axiovert 100TV, Zeiss) equipped with an HXP 120 lamp for epifluorescence illumination, a Coolsnap-HQ2 camera (Photometrics), a filter wheel (LUDL Electronic Products LTD), and electronic shutters driven by MetaMorph software (Molecular Devices Corp., Sunnyvale, CA, USA). Images were taken using either 63×/1.4 numerical aperture (NA) or 100×/1.4 NA Plan apochromatic oil objectives. Cells devoid of Hem1/Hem2 expression and thus incapable of lamellipodia formation served as tool to address and compare the effects of certain point mutations in either Hem1 or Hem2 on lamellipodia formation. Cells expressing respective construct (positive for EGFP signal) were categorized according to their cellular morphology as exemplified in "final figure C." Fractions of cells in percentage were plotted as stacked bar charts using Excel 2010 (Microsoft).

Video microscopy and immunofluorescence studies of patients and healthy controls

For details regarding immunofluorescence, TCR and BCR signaling analyses, and video microscopy, please refer to the Supplementary Materials.

Generation of Hem1$^{-/-}$ mice

To generate conditional Hem1-KO mice, a targeting vector was used in which exons 4 and 5 of the *Hem1* gene were flanked by loxP sites. A Neo-cassette flanked by frt sites was inserted into intron 3, allowing for G418 selection. This vector was electroporated into murine embryonic stem cells (embryonic stem line IGD3.2) (*25*). Homologous recombinant clones were identified by genomic Southern hybridization and polymerase chain reaction (PCR). A targeted embryonic stem cell clone was injected into C57BL/6 blastocysts and gave rise to germline chimeric animals. The Neo-cassette was removed from the hem1 locus by mating the resulting animals (fl_neo/wt), with transgenic mice expressing flip recombinase, resulting in conditional Hem1 mice (fl/wt) that were backcrossed to a C57BL/6 background. Last, male Hem1 fl/wt animals were crossed with female K14-cre mice to obtain animals being heterozygously deleted for Hem1 (del/wt). Unless otherwise indicated, age-matched female and male animals were used at 4 to 8 weeks of age. All mice were group-housed on a 12:12-hour light-dark cycles at 22°C with food and water provided ad libitum.

Bone marrow transplantation

Bone marrow transplantation studies were performed as previously described (*74*). In short, 8-week-old C57BL/6J mice were sublethally irradiated (2 × 6 Gy) and were subsequently intravenously injected via the retro-orbital plexus with 3×10^6 mixed bone marrow from 8-week-old J_HT and Hem1$^{+/+}$ versus Hem1$^{-/-}$ donors (4:1 ratio). The recipient mice were given a 14-week recovery period before intervention studies.

Microscopy

We further operated an Eclipse Ti-E (Nikon) inverted microscope system (setup #2) that was equipped with a high NA objective [×100 magnification, NA = 1.49, Nikon SR APO total internal reflection fluorescence (TIRF)] and a low NA objective (×20 magnification, NA = 0.75, Nikon S Fluor). For excitation, we used five diode lasers with the wavelengths 405, 488, 514, and 642 nm (iBeam smart, Toptica) and 532 and 561 nm (Obis). The excitation light was cleaned up with clean-up filters that matched the corresponding wavelengths (Chroma). Setup 2 was also coupled to a xenon lamp (Lambda LS lamp, Sutter Instrument Company), which was equipped with a filter wheel (Sutter Instrument Company) with the following filters installed: 340/26, 387/11, 370/36, 474/27, 554/23,

and 635/18 (all Chroma). This setup was further operated with the beam splitters zt405/488/532/640rpc and ET-Dualb. Sedat CFP (cyan fluorescent protein)/YFP (yellow fluorescent protein) sbxm + HC510/20 (all Chroma) and a Notch filter blocking 405-, 488-, 532-, and 640-nm light (Chroma). Emission light was cleaned up with the use of a filter wheel (Sutter Instrument Company), which was equipped with the bandpass filters ET450/50, ET510/20, ET525/50, ET605/52, and ET700/75 (all Chroma). Emission light was recorded with a backside-illuminated electron-multiplying charge-coupled device (EM-CCD) camera (Andor iXon Ultra 897). An eight-channel DAQ-card (National Instruments) and the microscopy automation and image analysis software MetaMorph (Molecular Devices) were used to program and apply timing protocols and control all hardware components. Microscopy setups were covered by a box, and temperature-sensitive experiments were conducted under the control of a temperature control system from Leica (setup #1) and PeCon (setup #2). For details regarding bilayer preparation and antibody labeling, please see the Supplementary Materials.

B cell synapse formation

Primary human B cells were washed once in imaging buffer [Hanks' balanced salt solution (HBSS) (Life Technologies) supplemented with ovalbumin (0.4 mg ml^{-1}; Merck), 2 mM $CaCl_2$, and 2 mM $MgCl_2$ (Merck)] and seeded on supported lipid bilayer (SLBs) functionalized with mSav:STAR635P-MHM88-biotin (20 to 100 molecules/μm^2) and intercellular adhesion molecule–1 (ICAM-1)–12His (~100 molecules/μm^2) to record B cell synapse formation. Images were recorded in TIRF mode using a 100× TIRF objective (Nikon) and at 25°C. We recorded B cell synapses only from adherent cells, a condition that was verified by interference reflection microscopy (IRM) using 554/23-nm lamp excitation and a CFP/YFP + HC510/20 cube. To visualize B cell synapse formation in TIRF, we recorded a red image (640-nm laser excitation, 705/72-nm emission filter) of mSav:STAR635P-MHM88-biotin followed by a blue image (488-nm laser excitation, 510/20-nm emission filter) of ICAM-1–AF488 with an illumination time of 10 ms. We used a laser power density of 0.16 and 0.06 kW cm^{-2} to excite STAR635P and AF488, respectively. Videos of B cell synapse formation were recorded with a 20× objective in epifluorescence mode using 635/18-nm lamp illumination to visualize mSav:STAR635P-MHM88-biotin, 474/27-nm lamp illumination to excite ICAM-1–AF488, and 554/23-nm lamp illumination to excite 7AAD (7-aminoactinomycin D) (live/dead cell discrimination). We recorded an image stack (whitelight, GFP, Cy3, and Cy5 illumination) every 10 s with an illumination time of 100 ms for all channels.

For experiments involving chemical fixation, cell samples were fixed with 4% PFA (Thermo Fisher Scientific) in PBS for 10 min at room temperature and subsequently washed in HBSS (Life Technologies) supplemented with ovalbumin (0.4 mg ml^{-1}; Merck), 2 mM $CaCl_2$, and 2 mM $MgCl_2$ (Merck) to terminate the fixation reaction. Microscopy images were processed and analyzed with the open-source image processing package Fiji (*75*). B cell synapse dynamics was assessed by measuring the ability of B cells to collect stimulatory anti-IgM antibodies (mSav:STAR635P-MHM88-biotin) upon interaction with the bilayer. For that purpose, the Fiji software was used to extract the area and the integrated density of fluorescently labeled anti-IgM (mSav:STAR635P-MHM88-biotin) associated with each cell. This analysis was applied to a sequence of 100 images covering an acquisition time of 34 min to capture both the spreading of individual B cell synapses and the progressive enrichment in collected anti-IgM antibodies.

SUPPLEMENTARY MATERIALS

immunology.sciencemag.org/cgi/content/full/5/49/eabc3979/DC1
Materials and Methods
Fig. S1. Defective WRC complex assembly and stability.
Fig. S2. T cell phenotype and function in human HEM1 deficiency.
Fig. S3. Extended B cell immunophenotyping in human HEM1 deficiency.
Fig. S4. Detailed characterization of $Hem1^{-/-}$ mice.
Fig. S5. Single-cell RNA-seq analyses of splenic T and B cell subclusters.
Fig. S6. Extended characterization of B cells and comparison with WASP-deficient B cells.
Table S1. Figure raw data.
Table S2. List of discriminating features for PCA of healthy donor and HEM1-deficient T cells upon fibronectin stimulation.
Table S3. T cell immunophenotyping in HEM1-deficient individuals compared with age-matched reference values.
Table S4. List of discriminating features for PCA of healthy donor and HEM1-deficient B cells upon IgM stimulation.
Table S5. B cell immunophenotyping in HEM1-deficient individuals compared with age-matched reference values.
Table S6. List of top differentially regulated genes in B cell subclusters as identified by 10× single-cell sequencing.
Table S7. List of top differentially regulated genes in T cell subclusters as identified by 10× single-cell sequencing.
Table S8. GO term enrichment of HEM1-deficient B cell functions derived from the top candidates from table S6.
Table S9. GO term enrichment of HEM1-deficient T cell functions derived from the top candidates from table S7.
Full Western blot scans for all figures.
References (*76*–*80*)

View/request a protocol for this paper from *Bio-protocol*.

REFERENCES AND NOTES

1. D. A. Moulding, J. Record, D. Malinova, A. J. Thrasher, Actin cytoskeletal defects in immunodeficiency. *Immunol. Rev.* **256**, 282–299 (2013).
2. W. H. A. Kahr, F. G. Pluthero, A. Elkadri, N. Warner, M. Drobac, C. H. Chen, R. W. Lo, L. Li, R. Li, Q. Li, C. Thoeni, J. Pan, G. Leung, I. Lara-Corrales, R. Murchie, E. Cutz, R. M. Laxer, J. Upton, C. M. Roifman, R. S. M. Yeung, J. H. Brumell, A. M. Muise, Loss of the Arp2/3 complex component ARPC1B causes platelet abnormalities and predisposes to inflammatory disease. *Nat. Commun.* **8**, 14816 (2017).
3. G. Lanzi, D. Moratto, D. Vairo, S. Masneri, O. Delmonte, T. Paganini, S. Parolini, G. Tabellini, C. Mazza, G. Savoldi, D. Montin, S. Martino, P. Tovo, I. M. Pessach, M. J. Massaad, N. Ramesh, F. Porta, A. Plebani, L. D. Notarangelo, R. S. Geha, S. Giliani, A novel primary human immunodeficiency due to deficiency in the WASP-interacting protein WIP. *J. Exp. Med.* **209**, 29–34 (2012).
4. S. Suetsugu, H. Miki, T. Takenawa, Identification of two human WAVE/SCAR homologues as general actin regulatory molecules which associate with the Arp2/3 complex. *Biochem. Biophys. Res. Commun.* **260**, 296–302 (1999).
5. K. G. Campellone, M. D. Welch, A nucleator arms race: Cellular control of actin assembly. *Nat. Rev. Mol. Cell Biol.* **11**, 237–251 (2010).
6. T. Takenawa, H. Miki, WASP and WAVE family proteins: Key molecules for rapid rearrangement of cortical actin filaments and cell movement. *J. Cell Sci.* **114**, 1801–1809 (2001).
7. C. Litschko, J. Linkner, S. Brühmann, T. E. B. Stradal, T. Reinl, L. Jänsch, K. Rottner, J. Faix, Differential functions of WAVE regulatory complex subunits in the regulation of actin-driven processes. *Eur. J. Cell Biol.* **96**, 715–727 (2017).
8. B. Chen, K. Brinkmann, Z. Chen, C. W. Pak, Y. Liao, S. Shi, L. Henry, N. V. Grishin, S. Bogdan, M. K. Rosen, The WAVE regulatory complex links diverse receptors to the actin cytoskeleton. *Cell* **156**, 195–207 (2014).
9. Z. Chen, D. Borek, S. B. Padrick, T. S. Gomez, Z. Metlagel, A. M. Ismail, J. Umetani, D. D. Billadeau, Z. Otwinowski, M. K. Rosen, Structure and control of the actin regulatory WAVE complex. *Nature* **468**, 533–538 (2010).
10. C. Yan, N. Martinez-Quiles, S. Eden, T. Shibata, F. Takeshima, R. Shinkura, Y. Fujiwara, R. Bronson, S. B. Snapper, M. W. Kirschner, R. Geha, F. S. Rosen, F. W. Alt, WAVE2 deficiency reveals distinct roles in embryogenesis and Rac-mediated actin-based motility. *EMBO J.* **22**, 3602–3612 (2003).
11. A. Wiskott, Familiärer, angeborener Morbus Werlhofii? *Monatsschr. Kinderheilkd.*, 212–216 (1937).

12. A. S. Mohan, K. M. Dean, T. Isogai, S. Y. Kasitinon, V. S. Murali, P. Roudot, A. Groisman, D. K. Reed, E. S. Welf, S. J. Han, J. Noh, G. Danuser, Enhanced dendritic actin network formation in extended lamellipodia drives proliferation in growth-challenged Rac1P29S melanoma cells. *Dev. Cell* **49**, 444–460.e9 (2019).
13. O. Moujaber, U. Stochaj, The cytoskeleton as regulator of cell signaling pathways. *Trends Biochem. Sci.* **45**, 96–107 (2019).
14. H. I. Brunner, M. Holland, M. W. Beresford, S. P. Ardoin, S. Appenzeller, C. A. Silva, F. Flores, B. Goilav, S. E. Wenderfer, D. M. Levy, A. Ravelli, R. Khunchandani, T. Avcin, M. S. Klein-Gitelman, B. M. Feldman, N. Ruperto, J. Ying; PRCSG and PRINTO Investigators, American College of Rheumatology provisional criteria for global flares in childhood-onset systemic lupus erythematosus. *Arthritis Care Res.* **70**, 813–822 (2018).
15. E. Beutler, G6PD deficiency. *Blood* **84**, 3613–3636 (1994).
16. S. Özen, E. D. Batu, S. Demir, Familial mediterranean fever: Recent developments in pathogenesis and new recommendations for management. *Front. Immunol.* **8**, 253 (2017).
17. M. Lek, K. J. Karczewski, E. V. Minikel, K. E. Samocha, E. Banks, T. Fennell, A. H. O'Donnell-Luria, J. S. Ware, A. J. Hill, B. B. Cummings, T. Tukiainen, D. P. Birnbaum, J. A. Kosmicki, L. E. Duncan, K. Estrada, F. Zhao, J. Zou, E. Pierce-Hoffman, J. Berghout, D. N. Cooper, N. Deflaux, M. DePristo, R. Do, J. Flannick, M. Fromer, L. Gauthier, J. Goldstein, N. Gupta, D. Howrigan, A. Kiezun, M. I. Kurki, A. L. Moonshine, P. Natarajan, L. Orozco, G. M. Peloso, R. Poplin, M. A. Rivas, V. Ruano-Rubio, S. A. Rose, D. M. Ruderfer, K. Shakir, P. D. Stenson, C. Stevens, B. P. Thomas, G. Tiao, M. T. Tusie-Luna, B. Weisburd, H.-H. Won, D. Yu, D. M. Altshuler, D. Ardissino, M. Boehnke, J. Danesh, S. Donnelly, R. Elosua, J. C. Florez, S. B. Gabriel, G. Getz, S. J. Glatt, C. M. Hultman, S. Kathiresan, M. Laakso, S. McCarroll, M. I. McCarthy, D. McGovern, R. McPherson, B. M. Neale, A. Palotie, S. M. Purcell, D. Saleheen, J. M. Scharf, P. Sklar, P. F. Sullivan, J. Tuomilehto, M. T. Tsuang, H. C. Watkins, J. G. Wilson, M. J. Daly, D. G. MacArthur; Exome Aggregation Consortium, Analysis of protein-coding genetic variation in 60,706 humans. *Nature* **536**, 285–291 (2016).
18. K. J. Karczewski, L. C. Francioli, G. Tiao, B. B. Cummings, J. Alföldi, Q. Wang, R. L. Collins, K. M. Laricchia, A. Ganna, D. P. Birnbaum, L. D. Gauthier, H. Brand, M. Solomonson, N. A. Watts, D. Rhodes, M. Singer-Berk, E. G. Seaby, J. A. Kosmicki, R. K. Walters, K. Tashman, Y. Farjoun, E. Banks, T. Poterba, A. Wang, C. Seed, N. Whiffin, J. X. Chong, K. E. Samocha, E. Pierce-Hoffman, Z. Zappala, A. H. O'Donnell-Luria, E. V. Minikel, B. Weisburd, M. Lek, J. S. Ware, C. Vittal, I. M. Armean, L. Bergelson, K. Cibulskis, K. M. Connolly, M. Covarrubias, S. Donnelly, S. Ferriera, S. Gabriel, J. Gentry, N. Gupta, T. Jeandet, D. Kaplan, C. Llanwarne, R. Munshi, S. Novod, N. Petrillo, D. Roazen, V. Ruano-Rubio, A. Saltzman, M. Schleicher, J. Soto, K. Tibbetts, C. Tolonen, G. Wade, M. E. Talkowski, The Genome Aggregation Database Consortium, B. M. Neale, M. J. Daly, D. G. MacArthur, Variation across 141,456 human exomes and genomes reveals the spectrum of loss-of-function intolerance across human protein-coding genes. bioRxiv 531210 [**Preprint**]. 30 January 2019.
19. A. Steffen, K. Rottner, J. Ehinger, M. Innocenti, G. Scita, J. Wehland, T. E. B. Stradal, Sra-1 and Nap1 link Rac to actin assembly driving lamellipodia formation. *EMBO J.* **23**, 749–759 (2004).
20. A. S. Rakeman, K. V. Anderson, Axis specification and morphogenesis in the mouse embryo require Nap1, a regulator of WAVE-mediated actin branching. *Development* **133**, 3075–3083 (2006).
21. S. Dolati, F. Kage, J. Mueller, M. Müsken, M. Kirchner, G. Dittmar, M. Sixt, K. Rottner, M. Falcke, On the relation between filament density, force generation, and protrusion rate in mesenchymal cell motility. *Mol. Biol. Cell* **29**, 2674–2686 (2018).
22. K. Dürre, F. C. Keber, P. Bleicher, F. Brauns, C. J. Cyron, J. Faix, A. R. Bausch, Capping protein-controlled actin polymerization shapes lipid membranes. *Nat. Commun.* **9**, 1630 (2018).
23. F. Kage, M. Winterhoff, V. Dimchev, J. Mueller, T. Thalheim, A. Freise, S. Brühmann, J. Kollasser, J. Block, G. Dimchev, M. Geyer, H.-J. Schnittler, C. Brakebusch, T. E. B. Stradal, M.-F. Carlier, M. Sixt, J. Käs, J. Faix, K. Rottner, FMNL formins boost lamellipodial force generation. *Nat. Commun.* **8**, 14832 (2017).
24. M. Schaks, S. P. Singh, F. Kage, P. Thomason, T. Klünemann, A. Steffen, W. Blankenfeldt, T. E. Stradal, R. H. Insall, K. Rottner, Distinct interaction sites of Rac GTPase with WAVE regulatory complex have non-redundant functions in vivo. *Curr. Biol.* **28**, 3674–3684.e6 (2018).
25. A. Leithner, A. Eichner, J. Müller, A. Reversat, M. Brown, J. Schwarz, J. Merrin, D. J. J. de Gorter, F. Schur, J. Bayerl, I. de Vries, S. Wieser, R. Hauschild, F. P. L. Lai, M. Moser, D. Kerjaschki, K. Rottner, J. V. Small, T. E. B. Stradal, M. Sixt, Diversified actin protrusions promote environmental exploration but are dispensable for locomotion of leukocytes. *Nat. Cell Biol.* **18**, 1253–1259 (2016).
26. Z. Zhu, Y. Chai, Y. Jiang, W. Li, H. Hu, W. Li, J.-W. Wu, Z.-X. Wang, S. Huang, G. Ou, Functional Coordination of WAVE and WASP in C. elegans Neuroblast Migration. *Dev. Cell* **39**, 224–238 (2016).
27. A. J. Squarr, K. Brinkmann, B. Chen, T. Steinbacher, K. Ebnet, M. K. Rosen, S. Bogdan, Fat2 acts through the WAVE regulatory complex to drive collective cell migration during tissue rotation. *J. Cell Biol.* **212**, 591–603 (2016).
28. A. Lanzavecchia, F. Sallusto, Antigen decoding by T lymphocytes: From synapses to fate determination. *Nat. Immunol.* **2**, 487–492 (2001).
29. E. J. H. Schatorjé, E. F. A. Gemen, G. J. A. Driessen, J. Leuvenink, R. W. N. M. van Hout, E. de Vries, Paediatric reference values for the peripheral T cell compartment: T lymphocyte subsets in children. *Scand. J. Immunol.* **75**, 436–444 (2012).
30. K. Minton, Innate lymphoid cells: Human ILCs face redundancy. *Nat. Rev. Immunol.* **16**, 596–597 (2016).
31. K. Bride, D. Teachey, Autoimmune lymphoproliferative syndrome: More than a FAScinating disease. *F1000Res.* **6**, 1928 (2017).
32. C. Schwab, A. Gabrysch, P. Olbrich, V. Patiño, K. Warnatz, D. Wolff, A. Hoshino, M. Kobayashi, K. Imai, M. Takagi, I. Dybedal, J. A. Haddock, D. M. Sansom, J. M. Lucena, M. Seidl, A. Schmitt-Graeff, V. Reiser, F. Emmerich, N. Frede, A. Bulashevska, U. Salzer, D. Schubert, S. Hayakawa, S. Okada, M. Kanariou, Z. Y. Kucuk, H. Chapdelaine, L. Petruzelkova, Z. Sumnik, A. Sediva, M. Slatter, P. D. Arkwright, A. Cant, H.-M. Lorenz, T. Giese, V. Lougaris, A. Plebani, C. Price, K. E. Sullivan, M. Moutschen, J. Litzman, T. Freiberger, F. L. van de Veerdonk, M. Recher, M. H. Albert, F. Hauck, S. Seneviratne, J. Pachlopnik Schmid, A. Kolios, G. Unglik, C. Klemann, C. Speckmann, S. Ehl, A. Leichtner, R. Blumberg, A. Franke, S. Snapper, S. Zeissig, C. Cunningham-Rundles, L. Giulino-Roth, O. Elemento, G. Dückers, T. Niehues, E. Fronkova, V. Kanderová, C. D. Platt, J. Chou, T. A. Chatila, R. Geha, E. McDermott, S. Bunn, M. Kurzai, A. Schulz, L. Alsina, F. Casals, A. Deyà-Martinez, S. Hambleton, H. Kanegane, K. Taskén, O. Neth, B. Grimbacher, Phenotype, penetrance, and treatment of 133 cytotoxic T-lymphocyte antigen 4–insufficient subjects. *J. Allergy Clin. Immunol.* **142**, 1932–1946 (2018).
33. A. B. Pernis, L. B. Ivashkiv, '-Omics' shed light on B cells in lupus. *Nat. Immunol.* **20**, 946–948 (2019).
34. A. Sharabi, G. C. Tsokos, T cell metabolism: New insights in systemic lupus erythematosus pathogenesis and therapy. *Nat. Rev. Rheumatol.* **16**, 100–112 (2020).
35. B. Piątosa, B. Wolska-Kuśnierz, M. Pac, K. Siewiera, E. Gałkowska, E. Bernatowska, B cell subsets in healthy children: Reference values for evaluation of B cell maturation process in peripheral blood. *Cytometry* **78B**, 372–381 (2010).
36. D. Lau, L. Y.-L. Lan, S. F. Andrews, C. Henry, K. T. Rojas, K. E. Neu, M. Huang, Y. Huang, B. DeKosky, A.-K. E. Palm, G. C. Ippolito, G. Georgiou, P. C. Wilson, Low CD21 expression defines a population of recent germinal center graduates primed for plasma cell differentiation. *Sci. Immunol.* **2**, eaai8153 (2017).
37. K. Thorarinsdottir, A. Camponeschi, I. Gjertsson, I.-L. Mårtensson, CD21low B cells: A snapshot of a unique B cell subset in health and disease. *Scand. J. Immunol.* **82**, 254–261 (2015).
38. L. Shao, J. Chang, W. Feng, X. Wang, E. A. Williamson, Y. Li, A. Schajnovitz, D. Scadden, L. J. Mortensen, C. P. Lin, L. Li, A. Paulson, J. Downing, D. Zhou, R. A. Hromas, The Wave2 scaffold Hem-1 is required for transition of fetal liver hematopoiesis to bone marrow. *Nat. Commun.* **9**, 2377 (2018).
39. E. A. Shikatani, R. Besla, S. Ensan, A. Upadhye, N. Khyzha, A. Li, T. Emoto, F. Chiu, N. Degousee, J. M. Moreau, H. M. Perry, D. Thayaparan, H. S. Cheng, S. Pacheco, D. Smyth, H. Noyan, C. C. J. Zavitz, C. M. T. Bauer, I. Hilgendorf, P. Libby, F. K. Swirski, J. L. Gommerman, J. E. Fish, M. R. Stampfli, M. I. Cybulsky, B. B. Rubin, C. J. Paige, T. P. Bender, C. A. McNamara, M. Husain, C. S. Robbins, c-Myb exacerbates atherosclerosis through regulation of protective IgM-producing antibody-secreting cells. *Cell Rep.* **27**, 2304–2312.e6 (2019).
40. A. E. Teschendorff, T. Enver, Single-cell entropy for accurate estimation of differentiation potency from a cell's transcriptome. *Nat. Commun.* **8**, 15599 (2017).
41. A. E. Teschendorff, P. Sollich, R. Kuehn, Signalling entropy: A novel network-theoretical framework for systems analysis and interpretation of functional omic data. *Methods* **67**, 282–293 (2014).
42. H. Park, K. Staehling-Hampton, M. W. Appleby, M. E. Brunkow, T. Habib, Y. Zhang, F. Ramsdell, H. D. Liggitt, B. Freie, M. Tsang, G. Carlson, S. Friend, C. Frevert, B. M. Iritani, A point mutation in the murine *Hem1* gene reveals an essential role for hematopoietic protein 1 in lymphopoiesis and innate immunity. *J. Exp. Med.* **205**, 2899–2913 (2008).
43. J. Chen, M. Trounstine, F. W. Alt, F. Young, C. Kurahara, J. F. Loring, D. Huszar, Immunoglobulin gene rearrangement in B cell deficient mice generated by targeted deletion of the JH locus. *Int. Immunol.* **5**, 647–656 (1993).
44. P. Shen, T. Roch, V. Lampropoulou, R. A. O'Connor, U. Stervbo, E. Hilgenberg, S. Ries, V. D. Dang, Y. Jaimes, C. Daridon, R. Li, L. Jouneau, P. Boudinot, S. Wilantri, I. Sakwa, Y. Miyazaki, M. D. Leech, R. C. McPherson, S. Wirtz, M. Neurath, K. Hoehlig, E. Meinl, A. Grützkau, J. R. Grün, K. Horn, A. A. Kühl, T. Dörner, A. Bar-Or, S. H. E. Kaufmann, S. M. Anderton, S. Fillatreau, IL-35-producing B cells are critical regulators of immunity during autoimmune and infectious diseases. *Nature* **507**, 366–370 (2014).
45. K. Minton, Recipe for a B cell. *Nat. Rev. Immunol.* **4**, 840 (2004).
46. N. S. De Silva, U. Klein, Dynamics of B cells in germinal centres. *Nat. Rev. Immunol.* **15**, 137–148 (2015).

47. J. Li, W. Yin, Y. Jing, D. Kang, L. Yang, J. Cheng, Z. Yu, Z. Peng, X. Li, Y. Wen, X. Sun, B. Ren, C. Liu, The coordination between B cell receptor signaling and the actin cytoskeleton during B cell activation. *Front. Immunol.* **9**, 3096 (2019).
48. D. Dominguez-Sola, J. Kung, A. B. Holmes, V. A. Wells, T. Mo, K. Basso, R. Dalla-Favera, The FOXO1 transcription factor instructs the germinal center dark zone program. *Immunity* **43**, 1064–1074 (2015).
49. H. S. Dengler, G. V. Baracho, S. A. Omori, S. Bruckner, K. C. Arden, D. H. Castrillon, R. A. DePinho, R. C. Rickert, Distinct functions for the transcription factor Foxo1 at various stages of B cell differentiation. *Nat. Immunol.* **9**, 1388–1398 (2008).
50. X. Zhang, N. Tang, T. J. Hadden, A. K. Rishi, Akt, FoxO and regulation of apoptosis. *Biochim. Biophys. Acta* **1813**, 1978–1986 (2011).
51. N. K. Serwas, B. Hoeger, R. C. Ardy, S. V. Stulz, Z. Sui, N. Memaran, M. Meeths, A. Krolo, Ö. Y. Petronczki, L. Pfajfer, T. Z. Hou, N. Halliday, E. Santos-Valente, A. Kalinichenko, A. Kennedy, E. M. Mace, M. Mukherjee, B. Tesi, A. Schrempf, W. F. Pickl, J. I. Loizou, R. Kain, B. Bidmon-Fliegenschnee, J.-N. Schickel, S. Glauzy, J. Huemer, W. Garncarz, E. Salzer, I. Pierides, I. Bilic, J. Thiel, P. Priftakis, P. P. Banerjee, E. Förster-Waldl, D. Medgyesi, W.-D. Huber, J. S. Orange, E. Meffre, D. M. Sansom, Y. T. Bryceson, A. Altman, K. Boztug, Human DEF6 deficiency underlies an immunodeficiency syndrome with systemic autoimmunity and aberrant CTLA-4 homeostasis. *Nat. Commun.* **10**, 3106 (2019).
52. A. Singh, V. Joshi, A. K. Jindal, B. Mathew, A. Rawat, An updated review on activated PI3 kinase delta syndrome (APDS). *Genes Dis.* **7**, 67–74 (2020).
53. O. Leavy, Mediators of central tolerance. *Nat. Rev. Immunol.* **15**, 404 (2015).
54. A. Stoddart, A. P. Jackson, F. M. Brodsky, Plasticity of B cell receptor internalization upon conditional depletion of clathrin. *MBoC* **16**, 2339–2348 (2005).
55. F. D. Batista, D. Iber, M. S. Neuberger, B cells acquire antigen from target cells after synapse formation. *Nature* **411**, 489–494 (2001).
56. E. Janssen, R. S. Geha, Primary immunodeficiencies caused by mutations in actin regulatory proteins. *Immunol. Rev.* **287**, 121–134 (2019).
57. N. S. Kolhatkar, A. Brahmandam, C. D. Thouvenel, S. Becker-Herman, H. M. Jacobs, M. A. Schwartz, E. J. Allenspach, S. Khim, A. K. Panigrahi, E. T. Luning Prak, A. J. Thrasher, L. D. Notarangelo, F. Candotti, T. R. Torgerson, I. Sanz, D. J. Rawlings, Altered BCR and TLR signals promote enhanced positive selection of autoreactive transitional B cells in Wiskott-Aldrich syndrome. *J. Exp. Med.* **212**, 1663–1677 (2015).
58. S. Becker-Herman, A. Meyer-Bahlburg, M. A. Schwartz, S. W. Jackson, K. L. Hudkins, C. Liu, B. D. Sather, S. Khim, D. Liggitt, W. Song, G. J. Silverman, C. E. Alpers, D. J. Rawlings, WASp-deficient B cells play a critical, cell-intrinsic role in triggering autoimmunity. *J. Exp. Med.* **208**, 2033–2042 (2011).
59. E. Janssen, H. Morbach, S. Ullas, J. M. Bannock, C. Massad, L. Menard, I. Barlan, G. Lefranc, H. Su, M. Dasouki, W. Al-Herz, S. Keles, T. Chatila, R. S. Geha, E. Meffre, Dedicator of cytokinesis 8–deficient patients have a breakdown in peripheral B-cell tolerance and defective regulatory T cells. *J. Allergy Clin. Immunol.* **134**, 1365–1374 (2014).
60. S. J. Keppler, F. Gasparrini, M. Burbage, S. Aggarwal, B. Frederico, R. S. Geha, M. Way, A. Bruckbauer, F. D. Batista, Wiskott-Aldrich syndrome interacting protein deficiency uncovers the role of the co-receptor CD19 as a generic hub for PI3 kinase signaling in B cells. *Immunity* **43**, 660–673 (2015).
61. E. Janssen, M. Tohme, M. Hedayat, M. Leick, S. Kumari, N. Ramesh, M. J. Massaad, S. Ullas, V. Azcutia, C. C. Goodnow, K. L. Randall, Q. Qiao, H. Wu, W. Al-Herz, D. Cox, J. Hartwig, D. J. Irvine, F. W. Luscinskas, R. S. Geha, A DOCK8-WIP-WASp complex links T cell receptors to the actin cytoskeleton. *JCI* **126**, 3837–3851 (2016).
62. M. Bolger-Munro, K. Choi, J. M. Scurll, L. Abraham, R. S. Chappell, D. Sheen, M. Dang-Lawson, X. Wu, J. J. Priatel, D. Coombs, J. A. Hammer, M. R. Gold, Arp2/3 complex-driven spatial patterning of the BCR enhances immune synapse formation, BCR signaling and B cell activation. *eLife* **8**, e44574 (2019).
63. A. Ozen, W. A. Comrie, R. C. Ardy, C. Dominguez Conde, B. Dalgic, O. F. Beser, A. R. Morawski, E. Karakoc-Aydiner, E. Tutar, S. Baris, F. Ozcay, N. K. Serwas, Y. Zhang, H. F. Matthews, S. Pittaluga, L. R. Folio, A. Unlusoy Aksu, J. J. McElwee, A. Krolo, A. Kiykim, Z. Baris, M. Gulsan, I. Ogulur, S. B. Snapper, R. H. J. Houwen, H. L. Leavis, D. Ertem, R. Kain, S. Sari, T. Erkan, H. C. Su, K. Boztug, M. J. Lenardo, CD55 deficiency, early-onset protein-losing enteropathy, and thrombosis. *N. Engl. J. Med.* **377**, 52–61 (2017).
64. E. Salzer, D. Cagdas, M. Hons, E. M. Mace, W. Garncarz, O. Y. Petronczki, R. Platzer, L. Pfajfer, I. Bilic, S. A. Ban, K. L. Willmann, M. Mukherjee, V. Supper, H. T. Hsu, P. P. Banerjee, P. Sinha, F. McClanahan, G. J. Zlabinger, W. F. Pickl, J. G. Gribben, H. Stockinger, K. L. Bennett, J. B. Huppa, L. Dupre, O. Sanal, U. Jager, M. Sixt, I. Tezcan, J. S. Orange, K. Boztug, RASGRP1 deficiency causes immunodeficiency with impaired cytoskeletal dynamics. *Nat. Immunol.* **17**, 1352–1360 (2016).
65. H. Müller, R. Jimenez-Heredia, A. Krolo, T. Hirschmugl, J. Dmytrus, K. Boztug, C. Bock, VCF. Filter: Interactive prioritization of disease-linked genetic variants from sequencing data. *Nucleic Acids Res.* **45**, W567–W572 (2017).
66. G. X. Y. Zheng, J. M. Terry, P. Belgrader, P. Ryvkin, Z. W. Bent, R. Wilson, S. B. Ziraldo, T. D. Wheeler, G. P. McDermott, J. Zhu, M. T. Gregory, J. Shuga, L. Montesclaros, J. G. Underwood, D. A. Masquelier, S. Y. Nishimura, M. Schnall-Levin, P. W. Wyatt, C. M. Hindson, R. Bharadwaj, A. Wong, K. D. Ness, L. W. Beppu, H. J. Deeg, C. McFarland, K. R. Loeb, W. J. Valente, N. G. Ericson, E. A. Stevens, J. P. Radich, T. S. Mikkelsen, B. J. Hindson, J. H. Bielas, Massively parallel digital transcriptional profiling of single cells. *Nat. Commun.* **8**, 14049 (2017).
67. F. A. Wolf, P. Angerer, F. J. Theis, SCANPY: Large-scale single-cell gene expression data analysis. *Genome Biol.* **19**, 15 (2018).
68. L. McInnes, J. Healy, J. Melville, UMAP: Uniform manifold approximation and projection for dimension reduction. arXiv:1802.03426 [stat.ML] (9 February 2018).
69. V. Traag, L. Waltman, N. J. van Eck, From Louvain to Leiden: Guaranteeing well-connected communities. *Sci. Rep.* **9**, 5233 (2019).
70. F. A. Wolf, F. K. Hamey, M. Plass, J. Solana, J. S. Dahlin, B. Göttgens, N. Rajewsky, L. Simon, F. J. Theis, PAGA: Graph abstraction reconciles clustering with trajectory inference through a topology preserving map of single cells. *Genome Biol.* **20**, 59 (2019).
71. M. Guo, E. L. Bao, M. Wagner, J. A. Whitsett, Y. Xu, SLICE: Determining cell differentiation and lineage based on single cell entropy. *Nucleic Acids Res.* **45**, e54 (2016).
72. N. Kolesnikov, E. Hastings, M. Keays, O. Melnichuk, Y. A. Tang, E. Williams, M. Dylag, N. Kurbatova, M. Brandizi, T. Burdett, K. Megy, E. Pilicheva, G. Rustici, A. Tikhonov, H. Parkinson, R. Petryszak, U. Sarkans, A. Brazma, ArrayExpress update—Simplifying data submissions. *Nucleic Acids Res.* **43**, D1113–D1116 (2015).
73. J. Schindelin, I. Arganda-Carreras, E. Frise, V. Kaynig, M. Longair, T. Pietzsch, S. Preibisch, C. Rueden, S. Saalfeld, B. Schmid, J. Y. Tinevez, D. J. White, V. Hartenstein, K. Eliceiri, P. Tomancak, A. Cardona, Fiji: An open-source platform for biological-image analysis. *Nat. Methods* **9**, 676–682 (2012).
74. A. C. Li, C. J. Binder, A. Gutierrez, K. K. Brown, C. R. Plotkin, J. W. Pattison, A. F. Valledor, R. A. Davis, T. W. Willson, J. L. Witztum, W. Palinski, C. K. Glass, Differential inhibition of macrophage foam-cell formation and atherosclerosis in mice by PPARα, β/δ, and γ. *J. Clin. Invest.* **114**, 1564–1576 (2004).
75. F. A. Ran, P. D. Hsu, J. Wright, V. Agarwala, D. A. Scott, F. Zhang, Genome engineering using the CRISPR-Cas9 system. *Nat. Protoc.* **8**, 2281–2308 (2013).
76. R. Houmadi, D. Guipouy, J. Rey-Barroso, Z. Vasconcelos, J. Cornet, M. Manghi, N. Destainville, S. Valitutti, S. Allart, L. Dupré, The Wiskott-Aldrich syndrome protein contributes to the assembly of the LFA-1 nanocluster belt at the lytic synapse. *Cell Rep.* **22**, 979–991 (2018).
77. M. Fairhead, D. Krndija, E. D. Lowe, M. Howarth, Plug-and-play pairing via defined divalent streptavidins. *J. Mol. Biol.* **426**, 199–214 (2014).
78. M. Howarth, D. J. Chinnapen, K. Gerrow, P. C. Dorrestein, M. R. Grandy, N. L. Kelleher, A. El-Husseini, A. Y. Ting, A monovalent streptavidin with a single femtomolar biotin binding site. *Nat. Methods* **3**, 267–273 (2006).
79. B. K. Rossboth, R. Platzer, E. Sevcsik, F. Baumgart, H. Stockinger, G. J. Schütz, J. B. Huppa, M. Brameshuber, Unscrambling fluorophore blinking for comprehensive cluster detection via PALM. bioRxiv 545152 [**Preprint**]. 30 May 2020.
80. V. Gudipati, J. Rydzek, I. D. Perez, L. Scharf, S. Königsberger, H. Einsele, H. Stockinger, M. Hudecek, J. B. Huppa, Inefficient ZAP70-signaling blunts antigen detection by CAR-T-cells. bioRxiv 720417 [**Preprint**]. 30 July 2019.

Acknowledgments: We acknowledge the patients and parents for their participation in the study. M. Busslinger provided J_HT KO mice to C.J.B. for further breeding and bone marrow transplantation experiments. We thank S. Allart and A. Canivet from the CPTP Cell Imaging Facility in Toulouse. We also thank M. Busslinger for providing J_HT KO mice for bone marrow transplantation experiments. We thank B. Ransmayr for assistance with figure preparation. We thank T. Hirschmugl for graphical adaptation of the scheme shown in Fig. 7G. **Funding:** The research leading to these results has received funding from the European Research Council Consolidator Grant iDysChart (ERC grant agreement number: 820074) (to K.B.), the FWF through project FWF I2250-B28 (to K.B. and E.S.), a Science Award of the Austrian Society of Pediatrics and Adolescent Medicine (to E.S.), grants by the Deutsche Forschungsgemeinschaft (to T.E.B.S. and K.R.), and intramural funding from the Helmholtz Society (to T.E.B.S.).
Author contributions: E.S., S.Z., and C.R. performed most experiments, analyzed data, and interpreted results. E.S. supervised C.R. S.Z. identified the mutation in *HEM1*. M.G.K., E.S., and S.Z. designed, performed, and analyzed murine immune phenotyping and transplantation experiments. P.H. and T.E.B.S. provided Hem1$^{-/-}$ mice originally generated in laboratory. S. Stahnke performed initial characterizations of Hem1$^{-/-}$ mice, was responsible for genotyping, and, together with P.H., supervised breeding and delivery of Hem1$^{-/-}$ mice for further analyses. F.K. generated Nap1/Hem1 double-KO B16-F1 melanoma cells and performed all experiments in this cell type. S. Stahnke performed dsDNA and cytokine analyses in Hem1$^{-/-}$ mice. M.C., together with J.M., performed CellProfiler analyses. D.M. provided critical input and performed initial mouse experiments. L.D. performed video microscopy analyses and provided critical intellectual input. B.H., R.C.A., and J.B. performed selected experiments. R.P. performed lipid bilayer experiments with S.Z., supervised by J.B.H. R.K. performed histological analyses and electron microscopy of Hem1$^{-/-}$ mice. K.R. and T.E.B.S. supervised F.K. and S. Stahnke and provided critical input to experiments and

manuscript. N.R. and S.Z. coordinated the study in Tehran. N.R., V.Z., and S. Shahkarami provided local infrastructure in Tehran, cared for the patients, and identified the family. C.J.B. provided laboratory resources for mouse experiments, supervised M.G.K., and provided critical intellectual input. A.L. and M.S. provided critical intellectual input. M.H. analyzed 10× single-cell RNA-seq data together with C.B., S.Z., and E.S. with input from C.S. K.B., E.S., S.Z., and A.L. wrote the manuscript together with input from C.R. and M.G.K. K.B. coordinated the study, provided laboratory resources, interpreted data, and took overall responsibility for the study. All of the authors provided critical input and agreed to this publication. **Competing interests:** The authors declare that they have no competing financial interests. **Data and materials availability:** All single-cell RNA-seq data included in this manuscript have been deposited with the functional genomics data store ArrayExpress archive and are accessible under the accession number E-MTAB-8706. Parts of Figs. 3 and 4 were created using the BioRender software. Correspondence and requests for materials should be addressed to kaan.boztug@ccri.at.

Submitted 23 April 2020
Accepted 4 June 2020
Published 10 July 2020
10.1126/sciimmunol.abc3979

Citation: E. Salzer, S. Zoghi, M. G. Kiss, F. Kage, C. Rashkova, S. Stahnke, M. Haimel, R. Platzer, M. Caldera, R. C. Ardy, B. Hoeger, J. Block, D. Medgyesi, C. Sin, S. Shahkarami, R. Kain, V. Ziaee, P. Hammerl, C. Bock, J. Menche, L. Dupré, J. B. Huppa, M. Sixt, A. Lomakin, K. Rottner, C. J. Binder, T. E. B. Stradal, N. Rezaei, K. Boztug, The cytoskeletal regulator HEM1 governs B cell development and prevents autoimmunity. *Sci. Immunol.* **5**, eabc3979 (2020).